Energy-Harvesting Performance of an Aircraft Propeller

Nederlof, R.; Ragni, D.; Sinnige, T.

DOI
10.2514/1.C038005

Publication date
2025

Published in
Journal of Aircraft

Citation (APA)
Nederlof, R., Ragni, D., & Sinnige, T. (2025). Energy-Harvesting Performance of an Aircraft Propeller. *Journal of Aircraft*, *62*(2), 349-369. https://doi.org/10.2514/1.C038005

JOURNAL OF AIRCRAFT
Vol. 62, No. 2, March–April 2025

Energy-Harvesting Performance of an Aircraft Propeller

Robert Nederlof,* Daniele Ragni,† and Tomas Sinnige‡
Delft University of Technology, 2629 HS Delft, The Netherlands

https://doi.org/10.2514/1.C038005

The electrification of aircraft is strongly coupled with the use of propellers as a propulsion system because of their high efficiency and their convenient integration with electric motors. Due to the operational flexibility of electric motors, the propeller can also be used in alternative operations, such as negative thrust and power mode. By operating the propeller at negative inflow angles at the blade segments, the torque and thrust are in the opposite direction compared to the conventional positive thrust conditions. This can be useful for control purposes or for energy harvesting. An experimental investigation was carried out to explain the physics behind the aerodynamic performance of a propeller at both positive thrust and energy-harvesting operation. Next to the measured integrated forces and moments on the propeller, stereoscopic particle image velocimetry was used to analyze the flowfield around the blades as well as the slipstream behind the propeller disk to identify the dominating flow phenomena that drive the energy-harvesting operation. The highly cambered blade sections for this typical aircraft propeller do not operate efficiently in energy-harvesting mode due to the associated negative angles of attack. The thin tip blade sections experience separated flow in these conditions, reducing the useful output power, compared to wind turbines, which feature opposite camber. To maximize the output power in the energy-harvesting conditions, a low pitch setting is required in combination with a relatively high advance ratio. However, this also comes at a cost of large negative thrust (drag) values.

Nomenclature

A	=	propeller disk area; πR^2, m^2
C_d	=	sectional drag coefficient
C_l	=	sectional lift coefficient
C_P	=	power coefficient; $P/(\rho n^3 D^5)$
C_p	=	pressure coefficient
C_Q	=	torque coefficient; $Q/(\rho n^2 D^5)$
C_q	=	sectional torque coefficient
C_T	=	thrust coefficient; $T/(\rho n^2 D^4)$
C_t	=	sectional thrust coefficient
c	=	chord of blade section, m
D	=	propeller diameter, m
F	=	functional value
f	=	focal length (f-stop)
J	=	advance ratio; $V_\infty/(nD)$
M_{tip}	=	tip Mach number
n	=	propeller rotational speed, Hz
P	=	propeller power; ωQ, W
P_C	=	power coefficient; $P/(\rho V_\infty^3 D^2)$
p	=	pressure, Pa
Q	=	torque, N·m
Q_C	=	torque coefficient; $Q/(\rho V_\infty^2 D^3)$
q	=	dynamic pressure, Pa
R	=	propeller radius, m
r	=	radial coordinate, m
Re	=	Reynolds number
T	=	thrust force, N
T_C	=	thrust coefficient; $T/(\rho V_\infty^2 D^2)$
V	=	velocity, m/s
x	=	streamwise coordinate, m
y	=	lateral coordinate, m
z	=	vertical coordinate, m
α	=	blade angle of attack, deg
β	=	blade pitch angle, deg
γ	=	propeller angle of attack, deg
η_{eh}	=	energy-harvesting efficiency; $-P/((\rho/2)V_\infty^3 A)$
η_{p}	=	propeller efficiency; TV_∞/P
η_{t}	=	turbine efficiency; $P/(TV_\infty)$
λ	=	tip speed ratio; $\omega R/V_\infty$
ρ	=	air density, kg/m^3
φ	=	propeller circumferential coordinate, deg
ϕ	=	velocity inflow angle, deg
ω	=	propeller rotational speed; $2\pi n$, rad/s
ω_z	=	z-vorticity; $\partial V_y/\partial x - \partial V_x/\partial y$, 1/s

Subscripts

a	=	axial (velocity)
eff	=	effective (velocity)
rel	=	relative (velocity)
s	=	static (pressure)
t	=	tangential (velocity)
t	=	total (pressure)
$0.7R$	=	at 70% blade radius
∞	=	freestream

Partially Presented as Paper 2022-3893 at the AIAA AVIATION 2022 Forum, Chicago, IL, June 27–July 1, 2022; received 22 March 2024; accepted for publication 16 January 2025; published online 7 March 2025.

*Ph.D. Candidate, Flight Performance and Propulsion Section, Faculty of Aerospace Engineering; r.nederlof-1@tudelft.nl.

†Associate Professor, Wind Energy Section, Faculty of Aerospace Engineering; d.ragni@tudelft.nl.

‡Assistant Professor, Flight Performance and Propulsion Section, Faculty of Aerospace Engineering; t.sinnige@tudelft.nl.

I. Introduction

PROPELLERS reemerge in novel aircraft designs in an attempt to reduce the climate impact of aviation. Propellers are easily combined with electric motors, which helps in the electrification of aviation. The scalability of electric motors allows for alternative positioning of the propellers on the airframe, resulting in distributed propulsion concepts. The increased design freedom associated with electric aircraft offers potential integration benefits, which can be exploited to improve the complete system performance [1,2]. Clever integration of the propulsion system with the wing could yield lift augmentation, drag reduction, and increased control authority by using asymmetric thrust. For novel aircraft designs, the propellers could also be used for different purposes than only to produce thrust. When propellers are set to produce negative thrust, they could in principle be used as an airbrake to steepen descent and hence reduce community noise. Furthermore, when the propellers generate negative thrust, they can be used as wind turbines to harvest energy during

phases of the flight where energy input is not required, such as during descent, where the electric motor could operate as a generator [3,4]. This energy harvesting process may decrease the total energy required for the aircraft, depending on the flight mission.

Pipistrel tested the energy-harvesting performance of their Alpha Electro through full-scale flight tests [5]. A 19% reduction in net energy consumption was observed when using the propeller in energy-harvesting operations. However, it must be noted that these results were obtained for a small aircraft that is specifically designed to perform training missions, and hence the takeoff and landing phases are long compared to the cruise phase, which allows for a relatively large energy recovery. For commercial aircraft, where the climb and/or cruise phases dominate the mission energy consumption, the possible relative savings will be less, especially with current battery technology.

The aerodynamics of both propellers and wind turbines are well understood when they are operating in their own conventional regime. However, using propellers in negative thrust and power conditions will mean that the blades are operating in off-design conditions, considering that they are designed to maximize efficiency in positive thrust conditions (takeoff, climb, and cruise combined). Conventional propellers are designed with negative thrust operations taken into account, but just for thrust reverse during ground operation, where the aerodynamic efficiency is not of importance. Furthermore, the effect of the off-design operation of a conventional propeller is often only considered when engine-inoperative conditions are analyzed. However, when propellers are used more often in off-design conditions, there is a need to quantify their aerodynamic performance. Furthermore, an installed propeller on an aircraft will not experience a straight inflow. The effects of this nonzero angle of attack of the propeller on the off-design performance are also unknown and need to be quantified.

A similar but opposite problem arises in airborne wind energy systems, where onboard power generation is implemented [6]. This "drag-power" concept was first explored by Makani Power [7], where the rotors on the aircraft were used primarily to harvest energy but were used occasionally as a propeller to take off, hover, or maneuver the aircraft. However, little to no research focuses on the specific aerodynamics of these dual-role rotors [8].

Due to the off-design operation of the propeller in energy-harvesting mode and associated strong flow separation on the blades, conventional numerical tools seem to be unable to accurately predict the performance in this mode. In the study of Goyal et al. [9], the off-design performance of the propeller in energy-harvesting mode was modeled using multiple methods with varying fidelity levels. For the energy-harvesting mode, large discrepancies between most of the numerical models and experimental results were found, and therefore an experimental approach was chosen for the research presented in this paper. The current study focuses on the isolated propeller performance, and the goal is to explain the physical phenomena that drive the performance in the off-design operation at negative loading conditions by analyzing the results obtained from model-scale wind tunnel experiments. This increased understanding can improve aircraft designs such that propellers can be used more efficiently for alternative purposes. This could lead to increased propulsion integration benefits for distributed propeller concepts. Moreover, operating the propeller in energy-harvesting conditions will invert the aerodynamic loads on the blade sections, and this inversion results in a reduction in axial velocity, and the swirl will have an opposite sign. Therefore, the propeller–wing interaction will also be altered, and the aerodynamic performance of the wing may be adversely affected. Insight into these slipstream phenomena will be important for future analyses of the performance of propeller–wing systems at negative thrust and power conditions.

II. Propeller Operation

The aerodynamics of propellers in the negative thrust regime are drastically different from those in the propulsive regime. A distinction is made between three different propeller operational modes: the propulsive, braking, and energy-harvesting modes. In Fig. 1, the velocity triangle and blade forces of a propeller blade section are shown for the different operational conditions, assuming a fixed blade pitch. Note that the loading arrows are not to scale (C_d is exaggerated). In this example, the different modes are achieved by changing the advance ratio, which changes the orientation of the effective velocity vector (V_{eff}). This change in propeller operation could also be achieved by decreasing the blade pitch for a fixed advance ratio. For the propulsive mode, there is a positive blade angle of attack (α), which results in positive sectional lift and hence positive thrust (see Fig. 1a). Note that small negative angles of attack are also possible if the blade sections are cambered. Furthermore, the propeller requires positive (input) power, which is provided by the motor. Note that the lift force primarily determines the thrust but also the torque on the blade section.

When the advance ratio is increased for a given blade pitch, there is a mode in which the thrust produced becomes negative, while a net power input is still needed, and this is referred to as the braking mode (see Fig. 1b). In the braking mode, there is a negative thrust force, while the torque is still positive, which means that power needs to be provided to create this negative thrust. The same situation can be achieved when the sectional lift is small in the negative sense. When the advance ratio is increased further, the energy-harvesting mode is achieved. In this mode, the thrust and the torque are both negative, even though the rotation direction remains unaltered compared to the propulsive mode (see Fig. 1c). This negative torque component leads to energy harvesting since it enables the electric motor to extract energy from the flow. The negative thrust and torque on the blade section will also greatly impact the induced velocities behind the blades in the propeller slipstream. As for a wind turbine, there will be a reduction in axial velocity behind the blades compared to an increase in axial velocity for the positive thrust case. Due to the negative direction of the torque force, the swirl velocity will be opposite compared to the positive thrust case.

The blades of conventional aircraft propellers are optimized for propulsive performance and thus feature positive camber, meaning that negative blade angles of attack are required for the highly cambered profiles to create the negative thrust and power. This means that the blade sections will be prone to flow separation at the negative angles of attack experienced in energy-harvesting mode, resulting in poor performance and unsteady phenomena such as vibrations. An initial wind tunnel experiment performed by Sinnige et al. [10] revealed a maximum energy-harvesting efficiency (η_{eh}) of a representative aircraft propeller of around 10%, which is

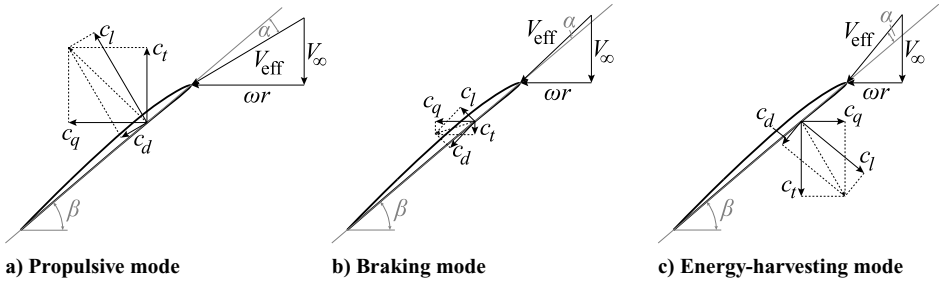

a) Propulsive mode **b) Braking mode** **c) Energy-harvesting mode**

Fig. 1 Velocity triangles and blade forces of a blade section in the propulsive, braking, and energy-harvesting modes for a fixed blade pitch (based on [10]).

significantly lower compared to the values reached by conventional wind turbines. The blade sections of wind turbine blades feature opposite camber compared to an aircraft propeller, such that the blade sections operate in positive loading conditions at high advance ratios. An alternative to using the propeller to harvest energy would be by pitching the propeller blade beyond 90° and inverting the rotational direction [11]. This would realign the camber with the local flow angle, similar to a wind turbine blade. However, this approach yields a pitch distribution over the blade span that is in the wrong direction, compared to a conventional propeller blade, meaning that the tip is twisted toward the freestream direction. Therefore, the root part will be loaded in a conventional way, now generating negative thrust and torque, while the tip part will generate negative lift, generating positive thrust and torque, counteracting the energy-harvesting performance of the root part of the blade. Furthermore, the need to flip the rotational direction during actual operation may make this option not as attractive as just operating the complete blade in energy-harvesting mode (Fig. 1c).

When the propeller is used to harvest energy, there will be a negative thrust force on the blades, as shown in Fig. 1c. This means that an aircraft that employs energy harvesting experiences more drag during the descent phase compared to conventional propeller operations. Due to this added drag, the descent trajectory has to become steeper, which in turn also means that the cruise phase has to become longer. Subsequently, this phase requires more energy, canceling part of the energy-harvesting benefit. Therefore, the net energy savings, when energy harvesting is implemented, heavily depend on the specific mission profile of the aircraft.

III. Experimental Methods

A. Wind Tunnel Setup and Model

To quantify the aerodynamic performance of a propeller that operates in both the propulsive and energy-harvesting modes, a wind tunnel experiment was performed in the Low-Turbulence Tunnel (LTT) at the Delft University of Technology. This is a low-speed closed-return wind tunnel and has an inflow turbulence level of around 0.02% for the selected freestream velocity of 30 m/s. The octagonal closed test section of 1.80 m × 1.25 m was used in which the propeller was placed in the center, while it was suspended from the ceiling, connected to the external balance. Regarding the uniformity of the inflow, the variation in freestream dynamic pressure over the cross-section at the measurement location in the vicinity of the propeller was at most ±0.05% [12], which equates to a maximum variation in freestream velocity of ±0.025%, which is less than 0.01 m/s for the used conditions. The external balance and hence the propeller setup could be rotated around the vertical axis to model a nonzero freestream angle of attack. Figure 2a displays a photograph of the test setup inside the test section as seen from the front. Figure 2b shows a technical drawing of the propeller setup, including relevant dimensions.

The TUD-XPROP propeller was used for the experiment, which is representative of a turboprop propeller in terms of disk and blade loading. However, three blades were removed from the original six-bladed propeller to limit power requirements in the propulsive regime while keeping a representative blade loading condition at reduced disk loading. This version of the propeller is referred to as the TUD-XPROP-3. Note that this propeller was not designed for operation at negative thrust and power conditions. The propeller has a diameter of 0.4064 m (16 in.) with a nacelle diameter of 0.0920 m (0.23D). The blades, which do not contain any sweep, are manufactured from carbon fiber. More information regarding the propeller blade geometry can be found in [13], and a CAD file of the test setup can be found on [14]. The round support sting was located at 491 mm (1.21D) from the propeller plane, to reduce the upstream effect of the sting on the blade performance. Furthermore, zigzag strips were placed on the support sting to trip the boundary layer to have a turbulent wake behind the sting. Finally, an aerodynamically designed aftcone was placed at the end of the nacelle to minimize the drag of the system. The blade pitch angle could be set manually up to an accuracy of ±0.1°. For this experimental campaign, the blade pitch angle was defined at 70% of the blade radius.

The propeller was operated with an electric motor, housed inside the nacelle. When the propeller was operated in energy-harvesting mode, the electric motor was used as a generator. The electric motor was driven by an electronic speed controller that was connected to a bidirectional power supply, such that the propeller could be controlled in both propulsive and energy-harvesting conditions. More details about the drive train layout can be found in [15], where an almost identical setup was used. An optical rotary encoder connected to the motor shaft was used to measure the rotational speed of the propeller. The signal from the encoder was used as input for the custom control software to control the rotational speed of the motor in both propulsive and energy-harvesting conditions. Using this software, the time-averaged rotational speed could be set with a

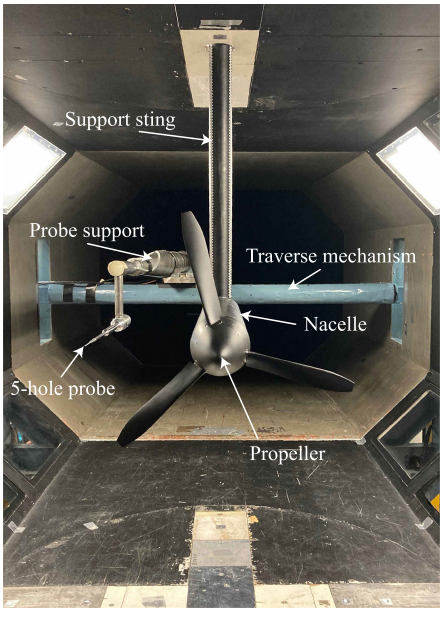

a) Overview of the test setup including main components

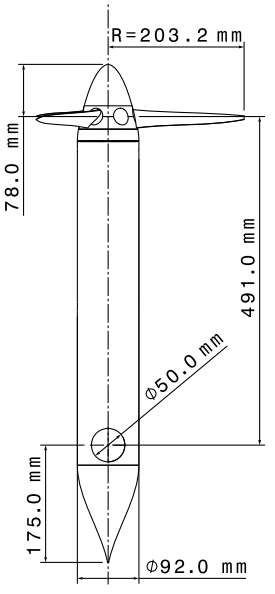

b) Top view including relevant dimensions

Fig. 2 Propeller test setup used in the experiment.

precision of ±0.01 Hz. Fluctuations in rotational speed at a given set point were measured to be 0.3% at most [15].

B. Measurement Techniques

1. External Balance and Load Cell

The propeller sting was connected to the six-component external balance of the wind tunnel (not depicted in Fig. 2a). Therefore, all system forces and moments, including that of the support structure, were measured by the external balance. The external balance has a high accuracy of around ±0.1 N and is hardly influenced by the operating conditions inside the test section, and therefore the external balance readings are practically unaffected by bias error due to temperature gradients. The external balance data were acquired at 10 Hz and averaged over 5 s of measurement time. The downside of using the external balance is that the propeller performance cannot be completely isolated. Measurements with the blades removed were performed to estimate the propeller-off performance of the support structure. However, there will always remain an additional sting-interference force component in the propeller-on readings, due to the interaction of the slipstream with the support structure, which cannot be isolated using the external balance alone.

To avoid this interaction component, an internal six-component load cell, mounted to the electric motor, was used to measure the isolated propeller performance. The load cell was calibrated for a full-scale load range of 480 N (± 0.07 N), 240 N (± 0.12 N), and 12 Nm (± 0.001 Nm) for thrust, in-plane forces, and torque, respectively. Again, more details about the load cell can be found in [15]. In every measurement run, the measurement sequence of the different advance ratios was randomized to convert potential drifts within a measurement run into random errors. The load cell data were acquired at 10 kHz and also averaged over 5 s per measurement. Additionally, repeated measurements were performed spanning multiple days and after configuration changes to verify the reproducibility of the readings. Due to temperature variations of the load cell inside the nacelle, caused by the heating of the electric motor, the strain gauge readings of the load cell were impacted. Since no temperature information of the load cell was available during the experiment, the temperature of the electric motor housing was used as an estimate of the load cell temperature. For a single measurement run, a linear fit between the starting and ending temperatures was used to correct for the drift in output readings due to the change in temperature.

Despite this correction method, the spread in thrust readings was found to be up to ±1 N, which is relatively large for the encountered measurement range and hence much more than the calibration uncertainty of the load cell. This was due to the relatively large impact of the temperature sensitivity of the strain-gauge bridge that is dominated by the thrust component. Since the encountered thrust values were small compared to the full range of the load cell, the error due to the temperature sensitivity becomes significant. By randomizing the order of the measurement points within runs and by sufficient repetition, the impact of the resulting measurement error on the overall performance trend was attempted to be minimized. To confirm that the large spread was caused by temperature effects rather than random errors in the actual propeller loading condition, the load cell thrust readings were compared with the external balance data in terms of thrust coefficient (C_T) versus advance ratio (J). Since the output readings from the external balance are not influenced by changes in motor temperature, the spread in C_T is expected to be much smaller than for the load cell data.

In Fig. 3, the raw C_T-data are shown for $\beta_{0.7R} = 15°$ and 30°, indicated by the markers. Each data set contained more than 200 data points, obtained during different runs. To describe the performance of the propeller in the considered J range, polynomial fits were used for the thrust and power coefficients. Note that 95% confidence intervals were added to the fitted curves but are indistinguishable from the fitted curves due to the large number of measurements performed, reducing the width of the intervals. To determine which degree of polynomials was needed for the different performance indicators, a t-test was performed for all coefficients for varying polynomial functions. The t-statistic for each coefficient was used to test the null hypothesis that the corresponding coefficient is zero against the alternative that it is different from zero, given the other predictors in the model. The degree of the polynomial was increased until the coefficient of the highest order term showed to be insignificant compared to the others. Fits were created for C_T and C_P, from which all other parameters were deduced. For $\beta_{0.7R} = 15°$, it was found that fourth- and third-degree polynomials were sufficient to fit the C_T and C_P data, respectively. For the higher pitch setting of $\beta_{0.7R} = 30°$, it was found that fifth- and sixth-degree polynomials were required for C_T and C_P, respectively. In Fig. 3a the load cell data are shown, while in Fig. 3b the thrust readings from the external balance are shown. The latter is defined as the net thrust of the balance by $T = T_{\text{prop-on}} - T_{\text{prop-off}}$. Note that the calculated thrust from the external balance will be different from the thrust from the load cell due to the slipstream-interaction component that cannot be isolated, as discussed before.

The spread in C_T load cell data for the $\beta_{0.7R} = 15°$ case is smaller than for $\beta_{0.7R} = 30°$, since the temperature could be controlled much better for the former, due to the lower shaft torque at this blade pitch setting. The external balance shows less spread than the load cell, which is primarily visible for the $\beta_{0.7R} = 30°$ case, confirming that the large spread is caused by the uncertainty in temperature calibration. The overall trends for the internal load cell data are similar to that of the external balance, confirming that the two ways of measuring the propeller thrust are analogous. Due to the high number of data points and resulting small confidence intervals, the used polynomial fits through the internal load cell data are expected to give the correct correlation between advance ratio and the thrust and torque coefficient. Furthermore, the spread for the torque was

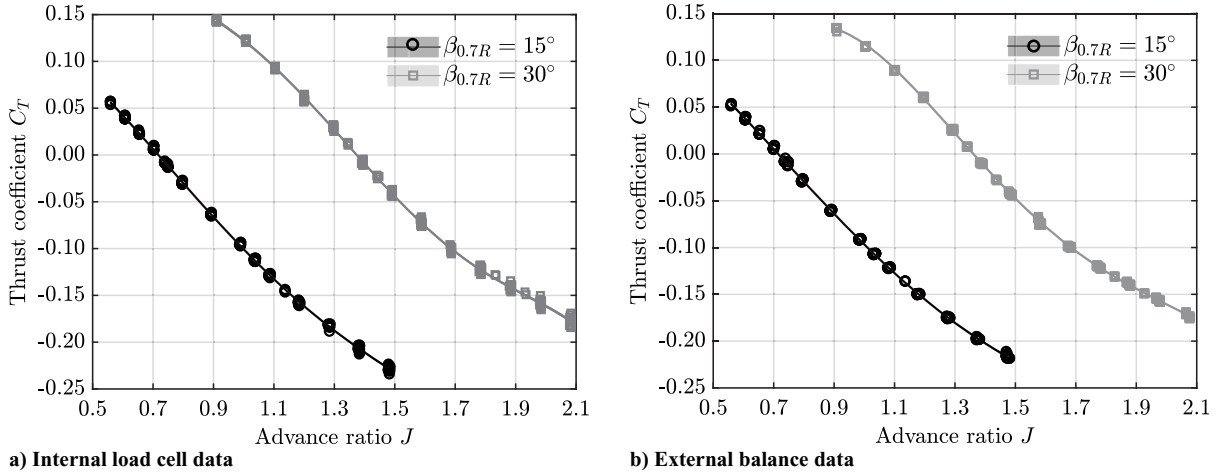

a) Internal load cell data **b) External balance data**

Fig. 3 Comparison between load cell and external balance thrust measurements for two different pitch settings.

found to be much smaller due to a lower temperature sensitivity of the strain gauge bridge dominated by the torque. Therefore, it was chosen to still use the internal load cell data for the assessment of the propeller performance in Sec. IV.

2. *Five-Hole Pressure Probe*

To obtain a better understanding of the observed integrated performance, a five-hole pressure probe was used to measure the total pressure inside the slipstream. The total pressure distribution measured close to the blades is representative of the loading distribution on the propeller blades. Furthermore, a Pitot tube was placed in front of the model at the side wall of the test section to measure the total and static pressure in the freestream. Both these probes were connected using flexible pressure tubes to a DTC Initium pressure scanner system. The pressures were averaged over the acquisition time of 5 s and were acquired at a sampling rate of 5 Hz. The measurement uncertainty of this system was given to be ±4 Pa from the calibration. The five-hole probe was used since it has a higher accuracy than a standard Pitot tube when there is a relatively large inflow angle (> 5°), which is the case in the propeller slipstream due to the swirl component. The layout of the five-hole probe is presented in Fig. 4a, together with a closed-up cut-through of the tip and the definition of the hole numbers [16]. The five-hole probe has a center hole, numbered as hole 5, and four surrounding holes. In the experiment, the probe was mounted such that holes number 1 and 3 were aligned with the vertical (z-) axis, while holes 2 and 4 were aligned with the lateral (y-) axis. The five-hole probe was calibrated using an elaborate calibration procedure in an empty tunnel, where combinations of angle of attack and angle of side-slip were set to the probe in the range of ±30°.

The measurements were performed in a plane of $1.0R \times 1.0R$ behind the blades parallel to the rotation axis, which is schematically shown in Fig. 4b. Note that the edge of the analysis plane was located at 3.0 mm behind the propeller rotational plane. In the analysis plane, 10 different streamwise rows were analyzed, with each containing 25 points in the direction of the blade span, adding up to a total of 250 points. The measurement points were closer together near the tip region to increase the spatial resolution near the slipstream boundary, since the largest gradients were expected there. The lowest spatial resolution in the radial direction was around 10 mm, close to the root part of the blade, while it was around 1 mm near the tip region of the blade. The 10 streamwise rows were spaced equally in the analysis plane, leading to a spatial resolution of around 20 mm in the streamwise direction.

3. *Particle Image Velocimetry*

To identify the relevant flow phenomena that drive the observed integrated performance, the velocity field around the propeller blades and inside the slipstream was analyzed. The flowfield around the different blade sections can be used to understand the observed integrated performance. Next to the flow around the blades, the velocity distributions in the slipstream will be different in the energy-harvesting mode, which may alter the performance of lifting surfaces submerged in the slipstream. Stereoscopic particle image velocimetry (PIV) was performed for both cases, and the PIV measurements were performed at the same operational conditions as for the five-hole probe measurements, such that the results could be compared. The tracer particles, created by a mixture of diethyleneglycol and water, were inserted into the tunnel. The 200 mJ Nd:YAG laser and two sCMOS cameras (16-bit 2560 px × 2160 px) were placed outside the test section, on a traversing system. For the phase-averaged measurements, 2000 uncorrelated image pairs were acquired, while for the phase-locked measurements, 500 image pairs were acquired. The main characteristics of the PIV setup are presented in Table 1. Note that the spatial resolution was calculated using the interrogation window size, excluding the overlap factor in the determination.

For the blade-sectional PIV, phase-locked measurements were performed, and these were triggered by the one-per-revolution signal from the optical encoder installed on the motor shaft to synchronize the image acquisition with the propeller blade position. These phase-locked PIV measurements were obtained in a horizontal plane, and the phase angle of the propeller blade was set to 90 deg with respect to this analysis plane, meaning that the laser sheet was perpendicular to the blade pitch axis (see Fig. 5a).

Due to limited optical access of the PIV setup, the blade-sectional PIV was performed with a single laser sheet, meaning that the rear side of the blade was not illuminated due to its own shadow, obstructing the reconstruction on this side of the propeller blade. This also meant that the PIV data could not be used to reconstruct pressure distributions [17]. The backside of the blades was fully illuminated. This side was chosen since the backside becomes the

Table 1 Characteristics of the PIV setups

Parameter	Blade-sectional analysis	Slipstream analysis
Laser type	Nd:YAG	
Camera type	sCMOS	
Objective	200 mm $f/8.0$	105 mm $f/5.6$
Field of view ($x \times y$)	$0.80R \times 0.85R$	$1.35R \times 1.15R$
Digital resolution	15.4 px/mm	16.9 px/mm
Image pairs phase-locked	500	500
Image pairs uncorrelated	N/A	2000
Image separation time	20 μs	
Interrogation window size	32 × 32 pixels	
Overlap factor	75%	
Spatial resolution	2.08 mm	1.89 mm
Maximum velocity uncertainty (mean)	3.2% V_∞	1.5% V_∞

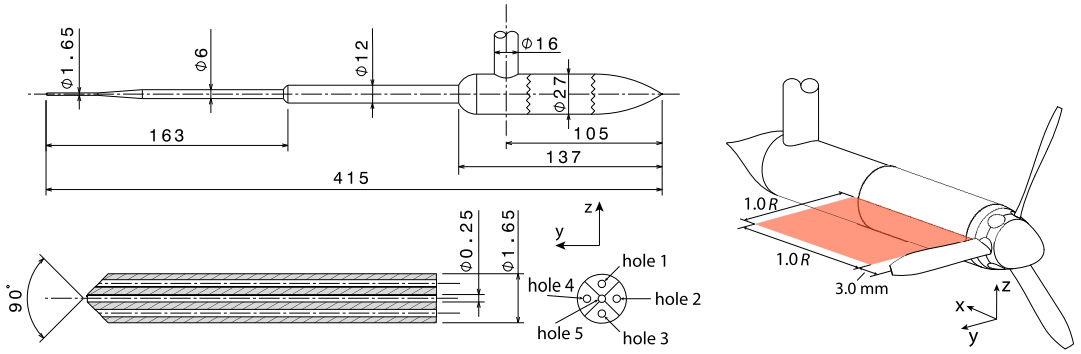

a) Layout of the 5-hole probe including dimensions in mm (derived from [16])

b) Analysis plane used for the 5-hole probe measurements

Fig. 4 Five-hole probe layout and measurement plane.

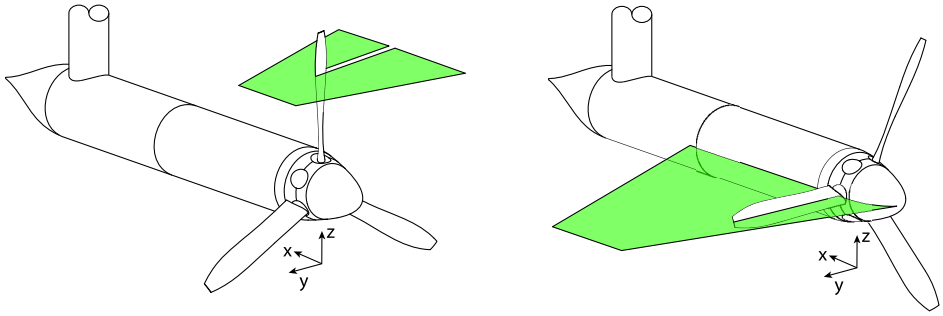

a) Blade-sectional analysis b) Slipstream analysis

Fig. 5 Position of the evaluation planes for the PIV analyses.

suction side during the energy-harvesting operations, and it was expected that the most dominating flow phenomena (e.g., separation) would occur here. The two cameras, equipped with 200 mm lenses, were positioned on the lower side of the test section on both lateral sides, such that both cameras were looking at the laser sheet from the bottom. The traverse mechanism allowed the whole setup to move up and down, such that multiple radial blade sections could be analyzed. A total of nine radial sections were analyzed, which were more densely spaced at the tip region than at the root (see Table 2). Only section number 1 was used to calibrate the setup due to calibration plate access, and it was assumed that the upward or downward movement of the setup did not influence the calibration.

For the slipstream analysis, the PIV analysis was performed in a plane behind the blades parallel to the propeller rotation axis, similar to the five-hole probe measurements (see Fig. 5b). Both phase-locked and phase-averaged measurements were performed for the slipstream analysis. For the former, the images were acquired with the phase angle of one of the blades set to 0 deg with respect to the analysis plane, meaning that one of the blades was centered around the laser sheet, as depicted in Fig. 5b. For the phase-averaged measurements, the blades were in some random position with respect to the analysis plane to have uncorrelated image sets. The mounting of the cameras and laser was altered for the slipstream analysis, such that the whole setup could move up- and downstream. This was done such that the complete evaluation plane was analyzed in two steps to increase the spatial resolution. The two cameras, for this analysis equipped with 105 mm lenses, were placed on a vertical fixture, and hence the cameras were looking from the top and bottom to the laser sheet while having the same streamwise position. The whole setup was then moved downstream while retaining the relative mounting of the cameras with respect to the laser sheet. The two frames were stitched together during the post-processing, leading to a field of view as denoted in Table 1.

C. Test Conditions

A large variation in operational conditions was tested to analyze the propeller performance in both propulsive and energy-harvesting modes. Furthermore, the propeller performance was measured for different propeller angle-of-attack (γ) values to quantify the performance at nonzero freestream angle-of-attack conditions. The pitch angle of the propeller blades is defined at 70% of the radius of the blades, and two different pitch settings were used in the experiment, namely, $\beta_{0.7R} = 15°$ and $\beta_{0.7R} = 30°$. The former is used since it was shown that lower pitch settings are more suitable for energy-harvesting purposes [10], while the latter is a representative pitch setting for operation at positive thrust. Higher pitch settings could not be achieved due to limitations in torque available. The freestream velocity was set to 30 m/s such that representative positive thrust settings could be achieved for the different pitch settings, given the limited maximum shaft torque from the motor.

Table 2 Propeller blade sections used for the blade-sectional analysis

Section	Radial position (r/R)
1	1.000
2	0.965
3	0.895
4	0.825
5	0.755
6	0.685
7	0.580
8	0.475
9	0.370

The propeller was operated in both propulsive and energy-harvesting conditions, and depending on the specific pitch setting, a different range of advance ratios was tested by varying the propeller rotational speed. At the beginning of each measurement run, the freestream velocity was set to 30 m/s for a fixed power input to the propeller. When varying the advance ratio of the propeller, the wind tunnel speed varied accordingly due to the change in propeller thrust. Furthermore, small temperature variations inside the wind tunnel during measurement runs altered the freestream velocity slightly, since the rpm of the wind tunnel fan was controlled, rather than the freestream dynamic pressure. During the experiment, changing the wind tunnel speed for each measurement point was deemed to be too time-consuming. Therefore, the wind tunnel speed was not exactly 30 m/s for each measurement point. Furthermore, the advance ratio varied slightly for repeated measurement points at the same rotational speed due to this approach. The maximum variation in freestream velocity was around $\pm 1.6\%$ for the most extreme positive and negative thrust cases. Due to the rotational speed component, the final variation in Reynolds number and Mach number at the blade sections due to varying freestream velocity was much smaller.

The overview of the considered conditions can be seen in Table 3. The lower bound on the advance ratio was mainly determined by the available power of the electric motor, while the upper bound was chosen such that a large portion of the energy-harvesting regime was tested, including the point of maximum energy output. Since the propeller operates as a wind turbine in the energy-harvesting phase, also the range of tip speed ratios (λ) is indicated, where $\lambda = \pi/J$. The wind tunnel operates at atmospheric conditions, and the relatively low freestream velocity used leads to low Reynolds and Mach numbers. Here, the Reynolds number was defined using the blade chord at 70% of the blade radius, and the Mach number was defined at the blade tip. Note that both were estimated without the induction effects taken into account. The full-size propeller will experience a much higher Reynolds and tip Mach number than the scaled propeller used in this experiment. The Reynolds number of a full-size turboprop propeller encountered during cruise conditions is at least one order of magnitude larger compared to values obtained during the experiment. Therefore, the observed performance and associated flow phenomena measured in the wind tunnel will differ from the full-size propeller. Observed flow phenomena during the experiments, such as flow separation, could be caused by the relatively low Reynolds number and therefore not fully representative of the full-scale propeller.

The same advance ratio sweeps as mentioned in Table 3 were performed at the propeller angles of attack ranging from $-20°$ to

Table 3 Overview of the analyzed test cases for the integrated performance measurements

Pitch angle	Advance ratio	Tip speed ratio	Reynolds number	Mach number
$\beta_{0.7R} = 15°$	$0.55 < J < 1.50$	$5.71 > \lambda > 2.09$	$1.07 \cdot 10^5 < Re_{0.7R} < 2.74 \cdot 10^5$	$0.20 < M_{\text{tip}} < 0.51$
$\beta_{0.7R} = 30°$	$0.90 < J < 2.10$	$3.49 > \lambda > 1.50$	$0.87 \cdot 10^5 < Re_{0.7R} < 1.75 \cdot 10^5$	$0.16 < M_{\text{tip}} < 0.32$

Table 4 Specific advance ratios and tip speed ratios for the blade and slipstream analysis

Pitch angle	Propulsive	Zero thrust	Energy harvesting
$\beta_{0.7R} = 15°$	$J = 0.60, \lambda = 5.24$	$J = 0.75, \lambda = 4.19$	$J = 1.10, \lambda = 2.86$
$\beta_{0.7R} = 30°$	$J = 1.20, \lambda = 2.62$	$J = 1.40, \lambda = 2.24$	$J = 1.90, \lambda = 1.65$

$+20°$ in steps of 2°. Both positive and negative propeller angles of attack were considered to check the symmetry of the experimental setup. For the advance ratio and propeller angle-of-attack ranges described, both the external balance and internal balance data were measured. Due to limited time in the wind tunnel, the slipstream analysis using the five-hole probe and the PIV analyses were only done for a selected number of operational conditions. For the two pitch angles, three different advance ratios were chosen at a propeller angle of attack of 0°. These advance ratios were approximately the point of maximum propeller efficiency, the point of zero thrust, and the point of maximum energy-harvesting efficiency. The corresponding values are given in Table 4. Note that these values were estimated a priori using blade element moment simulations [18].

D. Wind Tunnel Boundary Corrections

Since the propeller performance was measured in a closed wind tunnel, there are three blockage effects that modify the inflow velocity experienced by the propeller compared to the situation in an unbounded domain: solid blockage due to nacelle and support sting volume, wake blockage due to nacelle and sting drag, and propeller slipstream blockage. It was estimated that the blockage of the nacelle and sting combined resulted in an increase of about 0.5% of the effective freestream velocity. Depending on the thrust setting, the slipstream will contract or expand to various extents. At positive thrust settings, the contraction of the slipstream causes a decrease in the effective freestream velocity around the propeller. The slipstream blockage causes a decrease of about 0.6% of the effective freestream at the lower advance ratios, canceling the solid and wake blockage. At energy-harvesting settings, the expansion of the slipstream causes a further increase in the effective freestream velocity, adding to the solid and wake blockage. An additional increase of about 0.4% of the effective freestream is achieved at the highest advance ratios encountered due to the slipstream blockage. So at the maximum negative thrust settings, the increase of effective freestream velocity is about 0.9%. For the results presented in this paper, this difference was deemed negligible, especially since the uncertainty introduced by the temperature effects of the internal load cell resulted in larger variation in performance, and therefore the results were not corrected for the boundary effects.

IV. Propeller Performance

This section discusses the impact of operation at energy-harvesting conditions on the propeller performance. Firstly, the thrust and power, as well as efficiency values, are discussed. Secondly, the angle-of-attack effects on the propeller performance are discussed.

A. Propeller Thrust and Power

In this section, the integrated performance of the propeller is discussed for the straight propeller inflow case ($\gamma = 0°$). In Fig. 6, the aerodynamic performance of the propeller is shown in terms of the thrust coefficient (C_T) and the power coefficient (C_P) as a function of the advance ratio for the two considered pitch settings in Figs. 6a and 6b, respectively. For the pitch setting of $\beta_{0.7R} = 15°$, the thrust and power coefficients in the propulsive regime are almost linear with advance ratio, as is expected at these low loading conditions [19]. The thrust and power coefficients keep on decreasing with further increase in advance ratio because the blade inflow angle increases, which leads to a lower blade angle of attack for a given pitch setting (see Fig. 1). If the blade inflow angle becomes larger than the local pitch angle, it will lead to negative blade angles of attack on the blade sections. In the energy-harvesting regime, the C_T and C_P keep on decreasing with increasing advance ratio, also in a linear fashion for the first part. Finally, for higher advance ratios, the absolute thrust and power of the propeller in the energy-harvesting regime flatten or even reduce in magnitude due to the

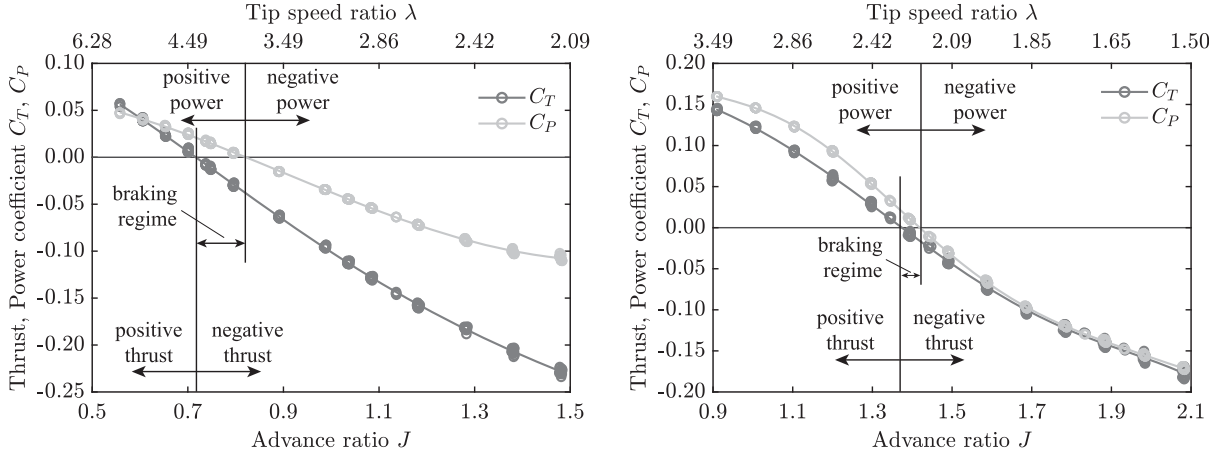

a) C_T and C_P versus advance ratio for $\beta_{0.7R} = 15°$ **b) C_T and C_P versus advance ratio for $\beta_{0.7R} = 30°$**

Fig. 6 Propeller performance for the two different pitch settings.

increasingly more negative blade angle of attack on the blade sections, which leads to separation on the blade sections, reducing the negative lift and hence the negative thrust. The kinks in the C_T curves in the energy-harvesting regime mark the end of the linear flow regime, meaning that the blade sections are close to stall. From this point onward, the negative thrust will increase marginally with increasing advance ratio until reaching the maximum negative thrust condition, after which the negative thrust will flatten or even reduce, as can be seen in the T_C versus advance ratio plot in Fig. 8a.

For the pitch setting of $\beta_{0.7R} = 15°$, a large part of the analyzed rotational speed range leads to negative thrust output of the propeller, caused by negative blade angles of attack on the blade, as shown in Fig. 1c. For a given pitch setting, the propeller enters the braking mode at a specific advance ratio, for which it starts to create negative thrust, while still requiring positive power. The braking mode spans a larger advance ratio domain for the lower pitch settings. This is due to the fact that, for the low pitch settings, the negative lift vector (C_l) obtained at small negative blade angles of attack is directed primarily in the direction of the thrust vector (C_t), as can be seen in Fig. 7a. When the advance ratio is increased and the inflow angle is increased, the negative lift vector will start to contribute more toward the negative torque, overcoming the opposing drag component. Thus, there is a relatively large change in blade inflow angle needed to enter the energy-harvesting mode for the low pitch setting.

The change in pitch to $\beta_{0.7R} = 30°$ shifts the $C_T - J$ curve horizontally toward higher advance ratios. For this higher pitch setting, the same thrust coefficient is reached at a higher advance ratio compared to the lower pitch setting. That means that, for a given C_T, the absolute disk loading is lower at the high pitch setting than at the lower pitch setting. When the pitch setting is increased, the nonlinear part of the $C_T - J$ curve starts to be visible. Since the induction is relatively low for the higher pitch setting, this nonlinearity is primarily caused by the large positive blade angles of attack on the blade sections, indicating a suboptimal operating range in the propulsive regime (beyond the maximum efficiency point).

The C_P curves show a linear behavior in low-thrust conditions, similar to the thrust coefficient. For the high-thrust settings, the power coefficient flattens, meaning that the required absolute power increases rapidly with a small decrease in advance ratio. This is also caused by the relatively low aerodynamic performance due to high positive blade angles of attack. At this higher pitch setting, the braking regime is more narrow in terms of the advance-ratio regime since the negative lift vector obtained at small negative blade angles of attack will already point largely in the direction of the negative torque, as can be seen in Fig. 7b.

For a fixed advance ratio (hence fixed blade inflow angle), a lower pitch setting leads to a higher negative thrust, since the blade angles of attack will be more negative than for a higher pitch setting. To more clearly analyze the change in negative thrust in the energy-harvesting regime with varying advance ratio, the T_C is plotted for the different pitch settings in Fig. 8a, where $T_C = C_T J^{-2}$. When the values of T_C are examined, it can be seen that the thrust becomes less negative again after the point of maximum negative thrust for the low pitch settings, while those of the high pitch setting remain more flat. This can also be explained by looking at Fig. 7. For a low pitch setting, any decrease in negative lift due to flow separation, with the increasingly negative blade angle of attack, will quickly decrease the negative thrust since the lift vector is directed in this direction. At the same time, the associated increase in drag does not contribute much to the negative thrust. However, for higher pitch settings, the same decrease in lift will be more compensated for by the increase in drag, due to the higher flow angle at which this stall is reached. This compensating effect becomes larger for higher advance ratios and hence explains the eventual flattening of the thrust curves. For a fixed negative blade angle of attack, and hence for a given C_l and C_d on the blade sections (ignoring Mach number and Reynolds number effects), a lower pitch setting will have a higher negative C_t and a lower C_q compared to a high pitch setting.

To have a further understanding of the performance at blade section level, the torque coefficient (Q_C) is plotted as a function of the advance ratio in Fig. 8b. For a fixed freestream, the Q_C is a

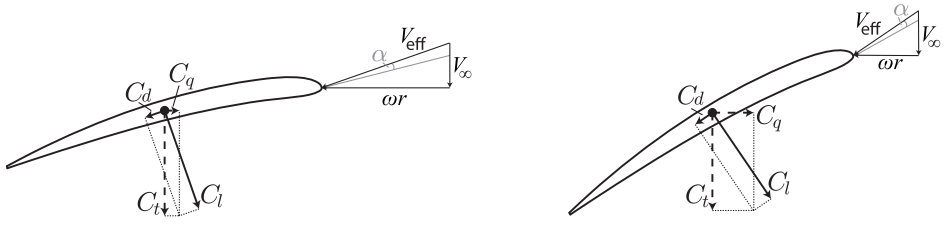

a) Low pitch setting, low advance ratio **b) High blade pitch setting, high advance ratio**

Fig. 7 Relevant blade forces during energy harvesting for different pitch settings assuming equal aerodynamic angle of attack.

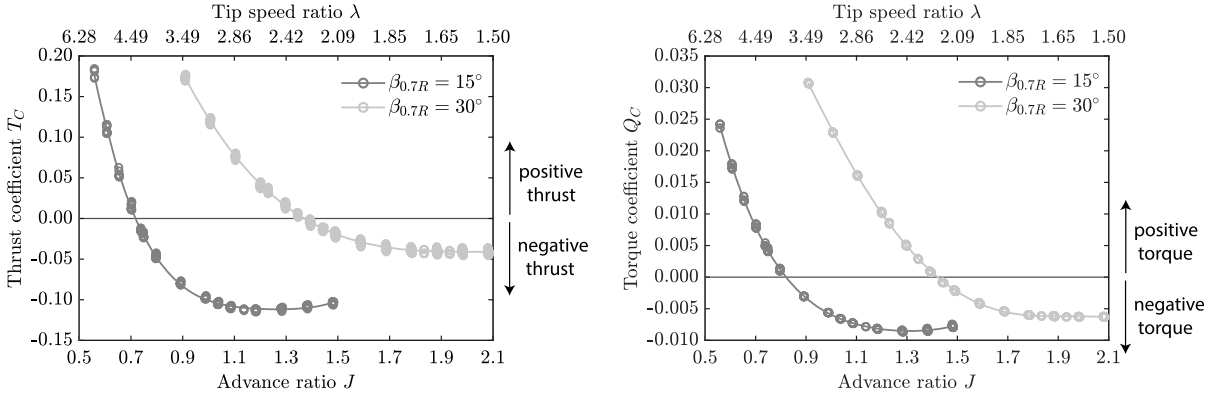

a) Thrust coefficient (T_C) versus advance ratio **b) Torque coefficient (Q_C) versus advance ratio**

Fig. 8 Propeller performance for the two different pitch settings.

direct measure of the absolute torque of the propeller, normalized in a similar way as T_C ($Q_C = C_Q J^{-2}$). Furthermore, the Q_C is directly related to the local 2D torque coefficient (C_q) of each blade section and therefore used here instead of P_C. As discussed before, when comparing two blade sections with the same aerodynamic angle of attack but with different pitch settings, the low pitch setting (Fig. 7a) would actually lead to a smaller negative C_q compared to the high pitch setting (Fig. 7b). However, this condition is reached for the low pitch setting at a lower advance ratio compared to the higher pitch setting. This means that the effective velocity is higher for the former, assuming the same freestream velocity, reducing the difference in Q_C between the two pitch settings. The sectional C_q and the integrated Q_C (or C_Q) are correlated by the ratio of effective velocity to the freestream velocity (see Eq. [1]).

$$Q_C \sim C_q \left(\frac{V_{\text{eff}}}{V_\infty}\right)^2 - > \left(\frac{V_{\text{eff}}}{V_\infty}\right)^2 = 1 + \left(\frac{\pi}{J}\frac{r}{R}\right)^2 \tag{1}$$

So even though the C_q is much smaller for a blade section at a low pitch setting compared to the high pitch setting, assuming an equal aerodynamic angle of attack, the difference in Q_C is reduced since the lower pitch settings achieved this condition at a higher relative velocity. This same reasoning explains why the difference in maximum negative T_C (Fig. 8a) between the two pitch settings is larger than the initial difference in blade-sectional C_t for a given aerodynamic condition. However, in this comparison, only one blade section is looked at, while the integrated performance is determined by the whole blade, leading to additional differences. Not all blade sections operate at the same aerodynamic angle of attack when comparing different pitch settings, due to the change in flow angle distribution of the blade with a change in advance ratio.

B. Efficiency

To minimize fuel consumption in the propulsive regime at a given thrust setting, the propeller efficiency should be maximized. In the propulsive regime, the efficiency of the propeller is defined as the ratio of thrust power over the shaft power ($\eta_p = TV_\infty/P$). The propeller efficiency for the propeller at the two tested pitch settings is shown in Fig. 9a. As is expected, the maximum propeller efficiency is larger for the case of $\beta_{0.7R} = 30°$ than for $\beta_{0.7R} = 15°$, since this condition is achieved at a lower thrust setting, which means lower axial induction losses. If the propeller is to be used for negative thrust, e.g., for stability and control, the produced thrust would be the only important performance parameter, while the power generated is of lower importance. However, in the energy-harvesting regime, the goal is to maximize the output power of the propeller and the previously defined propeller efficiency does not have any physical meaning. Instead, it is more relevant to analyze the amount of power that is being extracted from the freestream. Therefore, the energy-harvesting efficiency (η_{eh}) is defined as the amount of power extracted from the total available power of the incoming flow that passes through the propeller disk (A). The energy-harvesting efficiency is linked to the power coefficient (P_C) according to Eq. (2). This definition is analogous to the definition of the efficiency used in wind turbine design, where the upper limit is defined by the Betz limit of 59%.

$$\eta_{\text{eh}} = \frac{-P}{(1/2)\rho V_\infty^3 A} = -\frac{8}{\pi} P_C \tag{2}$$

In Fig. 9b, the energy-harvesting efficiency of the propeller is shown for both the pitch settings of $\beta_{0.7R} = 15°$ and 30°. For the higher pitch setting, the maximum energy-harvesting efficiency is reached at a higher advance ratio. From the data, it is confirmed that the energy-harvesting efficiency is rather low compared to equivalent wind turbines, similar to previous studies [10]. Firstly, the advance ratio is very high compared to wind turbine designs. The low advance ratio used by wind turbines means that the effective velocity is much higher for a given freestream velocity than for a propeller, leading to higher power output [Eq. (1)]. Secondly and more importantly, the low energy-harvesting efficiency is due to the blade design of this propeller, which is optimized for the propulsive mode. The highly cambered blade sections see large negative blade angles of attack in the energy-harvesting regime, which causes flow separation. This will be further analyzed when the total pressure distribution behind the blades is discussed together with the blade-sectional PIV results (see Sec. V). A lower pitch setting allows for more energy harvesting, and it seems that the maximum for $\beta_{0.7R} = 15°$ is about 11% of the total power present in the incoming flow.

The point of maximum energy-harvesting efficiency is approximately reached at the same blade angle of attack for the two pitch settings considered since the maximum power output is obtained close to the optimal (negative) sectional C_l/C_d. This can be explained by looking again at Fig. 7. For the energy-harvesting regime, the (negative) lift is directed in the negative torque direction, while the (positive) drag of the blade segments is directed in the positive torque direction, opposing the lift contribution. Increasing the advance ratio further could lead to an increase in negative lift coefficient; however, the reduction in effective velocity and the increase in drag associated with the increased negative blade angles of attack will offset the increase in negative lift in terms of the negative power. As mentioned before, the effective velocity (advance ratio) at which the aerodynamic blade forces are obtained is driving the integrated performance in terms of T_C and Q_C. When converting from torque to power, there is an additional factoring with the advance ratio ($P_C = 2\pi \cdot Q_C/J$). So even if the maximum negative Q_C would be the same for the two pitch settings, the lower pitch setting would have a higher energy-harvesting efficiency, since this condition is achieved at a lower advance ratio. For the energy-harvesting mode, the highest efficiency is achieved at a low pitch

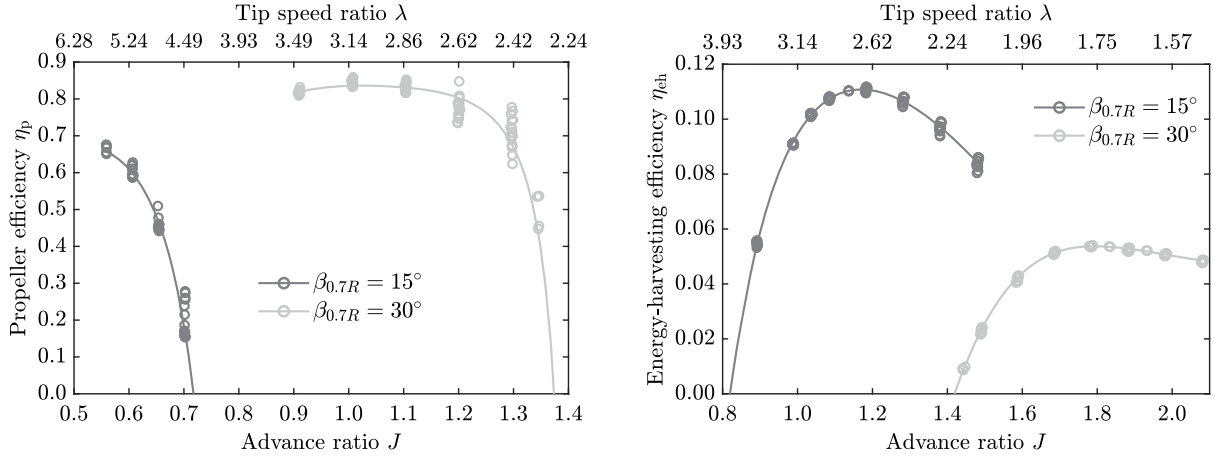

a) Propeller efficiency versus advance ratio **b) Energy-harvesting efficiency versus advance ratio**

Fig. 9 Propulsive and energy-harvesting efficiency for the two different pitch settings.

setting, while the propeller efficiency is highest for the higher pitch setting, meaning that a variable-pitch propeller should be used to be able to maximize both efficiencies in real flight.

When considering the use of energy-harvesting propellers on aircraft, the associated negative thrust (drag) is something that should be taken into account. Therefore, it would be also useful to analyze how efficiently the propeller can convert the blade forces (lift and drag) into negative power. To take this into account, a third efficiency is defined, called the turbine efficiency (η_t). The definition is shown in Eq. (3) and it is the inverse of the propeller efficiency definition. Note that both the propeller efficiency and turbine efficiency only apply in their associated operating window, so in propulsive mode, the turbine efficiency has no meaning (and vice versa).

$$\eta_t = \frac{-P}{-TV_\infty} = \frac{1}{\eta_p} \tag{3}$$

The turbine efficiency is a measure of the propeller's ability to extract power from the freestream, as a fraction of the drag power needed to reach this condition. The variation in turbine efficiency as a function of the advance ratio for the two tested pitch settings is shown in Fig. 10a.

The shape of the observed turbine efficiency curves is similar to those for the energy-harvesting efficiency, but now the highest pitch setting shows the highest maximum efficiency. This means that, for a given amount of drag, the propeller can more efficiently create negative power at a high pitch setting. The point of maximum turbine efficiency is achieved at a different advance ratio than the maximum energy-harvesting efficiency. In terms of aircraft design, it would be useful to know how much power can be extracted as a function of the allowable negative thrust. The energy-harvesting efficiency as a function of (negative) T_C is shown in Fig. 10b. For a fixed allowable negative thrust, the pitch setting can be found at which the propeller harvests the most power. Putting the propeller at $\beta_{0.7R} = 15°$ would lead to much higher negative thrust even for zero energy-harvesting power. This is another consequence of the large braking regime at the low pitch setting compared to the higher pitch setting, where the power only becomes negative when the negative thrust is already large. So even though the maximum energy-harvesting efficiency itself is higher at the low pitch setting, the associated negative thrust is even higher, reducing the turbine efficiency. Note that using the optimal η_{eh} during energy-harvesting does not necessarily mean the most harvested energy. If, for example, a lower negative T_C is chosen for the descent, the propeller has to operate at a lower energy-harvesting efficiency, but the total amount of harvested energy could be potentially more, due to a longer descent time compared to a higher negative T_C, highlighting the difficulty of choosing the right propeller operational condition at the aircraft design level.

C. Effect of Nonzero Propeller Angle of Attack

When the propeller is installed on a wing, the thrust axis is almost never aligned with the incoming freestream direction due to an overall angle of attack of the aircraft, a possible propeller installation angle, and the upwash generated by the wing. This means that the propeller will experience a nonzero inflow angle. At the aircraft design level, the thrust component of the propeller in the direction of the freestream is the relevant force to consider. However, in this study, the focus is put on the change in (isolated) propeller performance as a function of the propeller angle of attack, and hence the thrust is always the force aligned with the propeller axis. The performance at the angle of attack is compared to that at zero propeller angle of attack ($\gamma = 0°$).

For the performance curves shown in this section, fourth-order polynomials were fitted through the raw data. The 95% confidence intervals of the fits are also added but are sometimes very small due to the high certainty of the fit, especially for C_P. During the measurements for a given advance ratio, the positive propeller angles were tested first, after which the negative angles were assessed. Since the change in load cell temperature was most significant for the first data points for each advance ratio run, there is more spread observed between runs for the positive propeller angles, compared to the negative propeller angles, where the temperature change was less. Note that, for small propeller angles, the introduced uncertainty in the thrust data is of the same order as the variation due to the angle of attack. Furthermore, the case of $\gamma = 0°$ was repeated three times for each run, and hence there is even more scatter for the thrust readings at this propeller angle.

In Fig. 11, the performance results are shown for both positive and energy-harvesting conditions when changing the propeller angle of attack. The value on the y-axis is the relative change in performance (F) compared to the value at zero propeller angle of attack (F_0). So, irrespective of the sign of the thrust reading, a positive value indicates an increase in an absolute sense, while a negative value indicates a decrease in an absolute sense. Two specific advance ratios for the two pitch settings are shown for clarity. These two advance ratios were the point of maximum propeller efficiency and the point of maximum energy-harvesting efficiency for the case of $\gamma = 0°$, as presented in Table 4. For $\beta_{0.7R} = 15°$, the propulsive and energy-harvesting advance ratios are shown in Figs. 11a and 11b, respectively. As can be seen, the thrust becomes more positive when increasing the angle of attack of the propeller. This is true for both the propulsive and energy-harvesting regimes, which means that the thrust increases for the propulsive case, while it becomes less negative for the energy-harvesting case. The same is true for the power of the propeller. The value of the required power in the positive thrust regime is increased, while the value of the energy-harvesting power is reduced in the negative thrust regime.

Due to the relative angle of the freestream, there is a reduction of the rotational velocity on one side of the propeller, which leads to a

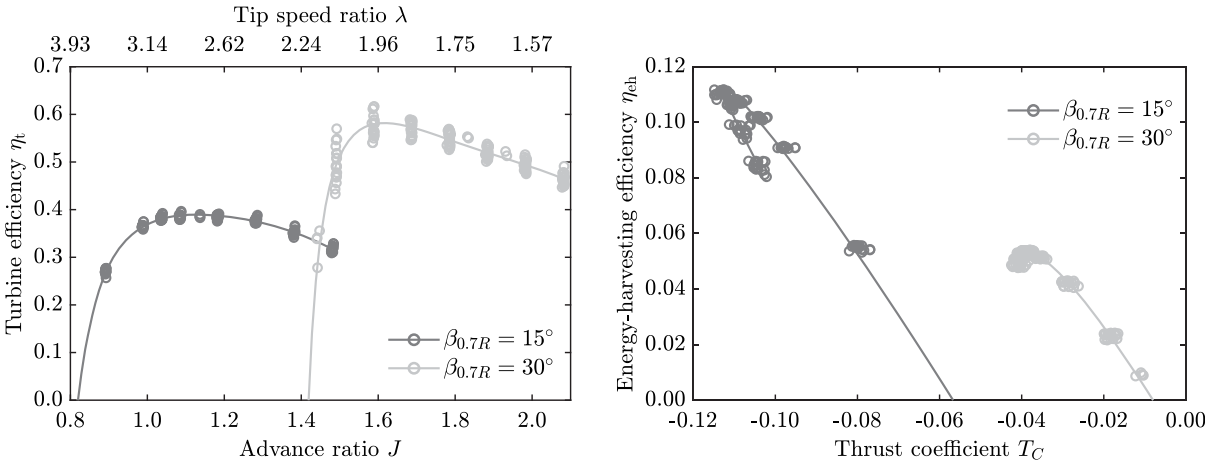

a) Turbine efficiency versus advance ratio **b) Energy-harvesting efficiency versus thrust coefficient**

Fig. 10 Efficiency in energy-harvesting conditions for the two different pitch settings.

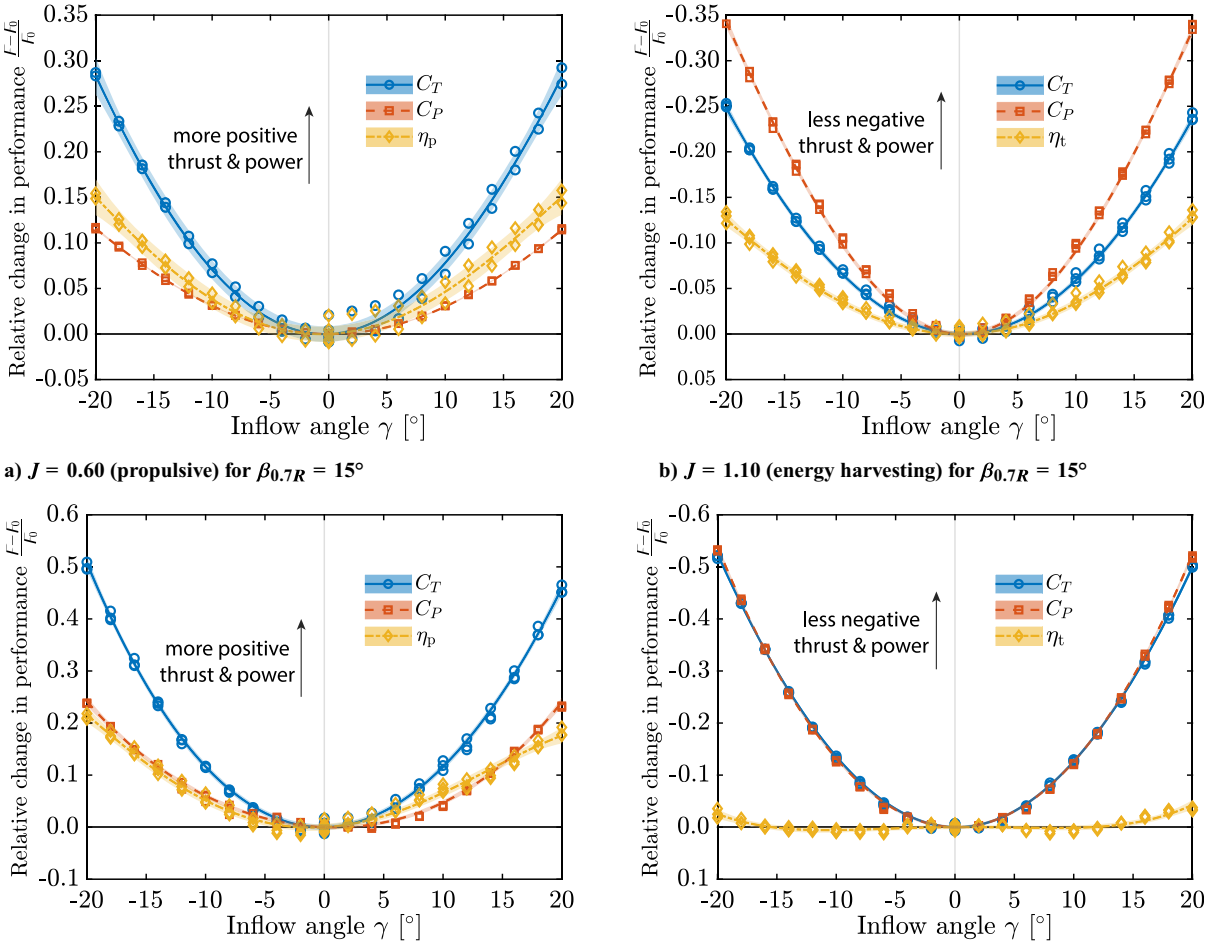

a) $J = 0.60$ (propulsive) for $\beta_{0.7R} = 15°$

b) $J = 1.10$ (energy harvesting) for $\beta_{0.7R} = 15°$

c) $J = 1.20$ (propulsive) for $\beta_{0.7R} = 30°$

d) $J = 1.90$ (energy harvesting) for $\beta_{0.7R} = 30°$

Fig. 11 Influence of the propeller angle of attack on the performance for both propulsive and energy-harvesting conditions.

decrease in both the local angle of attack and the effective velocity at the blade sections, both leading to smaller aerodynamic forces for the positive thrust condition. However, for the energy-harvesting condition, the decrease in the local angle of attack could potentially lead to higher negative C_l and C_d. This increase in aerodynamic performance is offset by the decrease in dynamic pressure in terms of absolute forces. On the other side of the propeller rotation, there is an increase in rotational velocity, increasing both the local angle of attack and effective velocity at the blade sections. For the positive thrust case, this potentially leads to a bigger sectional lift and drag, assuming that the increase in angle of attack would not lead to a significant reduction of C_l (separation). For the energy-harvesting case, the increase in angle of attack leads on this side to smaller negative C_l and C_d, which then again is offset by the increase in dynamic pressure. The magnitude of the increase or decrease in aerodynamic forces and hence thrust and torque on both sides together determine the overall change in propeller performance. It turns out that, for the tested conditions, there is an increase in thrust, irrespective of the thrust setting (positive and negative). The same can be said for the torque/power of the propeller, which is mainly driven by the component of lift in the direction of the torque at each blade section and thus behaves similarly as for the thrust component.

For the propulsive mode, the increase in thrust when varying γ is larger than the increase in power, increasing the propeller efficiency. However, for the energy-harvesting mode, the opposite is true, where the absolute reduction in negative thrust is smaller than the absolute reduction in power, leading to a turbine efficiency that becomes smaller with increasing propeller angle of attack. For the energy-harvesting mode, the absolute decrease in C_P directly relates to the decrease in η_{eh}, since less power is extracted from the flow. The outliers in terms of change in trust and therefore propeller efficiency for $J = 0.60$ at $\gamma = 0°$ are caused by the aforementioned temperature variations of the load cell. Note that only one of the six measurement points deviates from the general trend at $\gamma = 0°$, forcing the curve to be close to zero here regardless.

For the lower loaded propeller blades at $\beta_{0.7R} = 30°$, the increase in thrust with increasing propeller angle of attack in both regimes is more significant than for $\beta_{0.7R} = 15°$ (see Figs. 11c and 11d for the propulsive and energy-harvesting mode, respectively). At the most extreme propeller angles considered ($\gamma = \pm 20°$), the thrust changes up to 50% compared to the zero propeller angle of attack, becoming more positive for both the thrust regimes. Since the advance ratio is higher than for the $\beta_{0.7R} = 15°$ case, the rotational speed is relatively low compared to the freestream velocity. A change in the rotational velocity component induced by the propeller angle of attack will be therefore more significant than for the low pitch setting. Therefore, the change in power for $J = 1.20$ and $J = 1.90$ is also more than for $J = 0.60$ and $J = 1.10$, repetitively. For the propulsive case ($J = 1.20$), the further increase in thrust with increasing propeller angle compared to the lower pitch setting ($J = 0.60$) is more dominant than the further increase in power when comparing the two pitch settings, leading to a further increase in propeller efficiency at large propeller angles of attack for $\beta_{0.7R} = 30°$ compared to $\beta_{0.7R} = 15°$. At the energy-harvesting advance ratio ($J = 1.90$), the situation is different for the higher pitch setting compared to the lower pitch setting, since the relative decrease in thrust and power with increasing angle of attack is more or less equal. Therefore, there is hardly any change in turbine efficiency when varying the propeller angle of attack. This means that the relative reduction in negative lift and drag is more or less similar, leading to an equal reduction in negative thrust and torque (hence power).

V. Blade Performance

A. Blade Loading

To increase the understanding of the flow phenomena that drive the propeller performance, especially in the energy-harvesting regime, the five-hole pressure probe was used to analyze the total pressure distribution in the slipstream, close to the blades. The total pressure here can be used as an indicative value of the blade loading. However, the total pressure is related to the change in both axial and tangential velocity components, induced by the blade loading ($\Delta p_t \sim \Delta V_a + \Delta V_t$). When the propeller is generating negative thrust, there is an axial velocity deficit, which causes a reduction in total pressure. However, the tangential velocity induced by the torque will counteract part of this total pressure loss ($-\Delta p_t \sim -\Delta V_a + \Delta V_t$). So for a given energy-harvesting power, the reduction in axial velocity is to be minimized, reducing the total pressure loss. When examining the total pressure distribution on the blades, only the relative magnitude of the forces on the blade sections can be derived, but not the orientation of the local forces. The total pressure is expressed using the total pressure coefficient, which is defined as the following:

$$C_{p_t} = \frac{p_t - p_{t_\infty}}{q_\infty} \tag{4}$$

where p_{t_∞} is determined using the Pitot tube at the front of the test section and q_∞ is determined using the tunnel calibration. In Fig. 12 the total pressure distributions obtained using the five-hole probe are presented for the two pitch settings that were analyzed. These distributions were obtained at $0.15R$ downstream of the propeller plane. The analyzed advance ratios, as presented in Table 4, were expected to be representative of the maximum propeller efficiency point in the propulsive mode, the zero thrust point, and the maximum energy-harvesting power output point, respectively. As explained before, these advance ratios were estimated a priori using numerical simulations. It turned out that there were small deviations in terms of advance ratios at which the mentioned conditions actually occurred. For the low pitch setting, there was a small mismatch in the point of maximum energy harvesting, as can be seen in Fig. 9b. For the high pitch setting, both the zero-thrust and maximum energy-harvesting condition occur at a slightly lower advance ratio than estimated. However, the curves of thrust and power are rather flat in the range of these advance ratios, and hence the difference in performance is expected to be small between these two points.

Figure 12a shows that, at $\beta_{0.7R} = 15°$, the loading near the blade tip was negative for the propulsive case. This is due to the local negative angles of attack on the blade sections, reducing the propeller efficiency. The radial distribution of the local angle of attack on the blade sections is affected by blade twist, which for this propeller is optimized for a higher pitch setting than for $\beta_{0.7R} = 15°$, and hence the design advance ratio is also higher. Operating this propeller at a lower advance ratio in the propulsive mode leads to higher angles of attack at the root but more negative angles of attack at the tip compared to the design conditions. For the zero thrust condition, a large part near the root of the blade has a positive loading. At the same time, the whole outboard region, from 70% of the blade radius on, is negatively loaded. The integrated loading results in a close-to-zero net loading.

For the energy-harvesting mode, the total pressure distribution is rather flat over a large part of the blade span, indicating that the blade sections are operating at suboptimal performance. As mentioned before, the radial distribution of the blade section angle of attack is suboptimal due to the low pitch setting. Hence, in the energy-harvesting mode, the root region experiences more negative angles of attack compared to the tip sections at the low pitch setting. Furthermore, the negative peak at around 90–95% at the other advance ratios seems to have disappeared, possibly caused by separation on the blades. The separation causes a reduction in negative lift, while the drag increases, both reducing the negative torque. However, since the lift force is primarily oriented in the thrust direction, the negative thrust will also be reduced, reducing the loss in total pressure. To have a further understanding of the flow around the blade sections, the flowfield around the blade is quantified in Sec. V.B.

Numerical simulations performed by Goyal et al. [9,20] have shown that almost the complete blade has actually stalled at these energy-harvesting conditions, confirming the flat loading distribution observed. The peak in negative total pressure for the energy-harvesting case is at around 85% of the blade radius, which is significantly different compared to the propulsive case. This means that most of the negative thrust is created close to the tip region. However, this does not directly relate to efficient aerodynamic operation of these blade sections. In the energy-harvesting conditions, the drag component adds to the negative thrust (see Fig. 1c), and hence a blade section that has a low lift-to-drag ratio, could still yield a large negative thrust. To further understand how the loading is generated on the blade, the axial and tangential velocity fields behind the blades are discussed in Sec. VI.

In Fig. 12b, the results are shown for $\beta_{0.7R} = 30°$. The propulsive mode ($J = 1.20$) shows a positive total pressure distribution over the whole blade, indicating that the tip region is not negatively loaded, as was the case at the lower pitch setting, resulting in a higher propeller efficiency. It can also be observed that this maximum propeller efficiency is indeed obtained at a lower blade loading, resulting in fewer profile and induction losses compared to the low pitch setting. For the estimated zero thrust condition $J = 1.40$, almost the whole blade shows a negative loading, even though this loading is very small. In the energy-harvesting mode ($J = 1.90$),

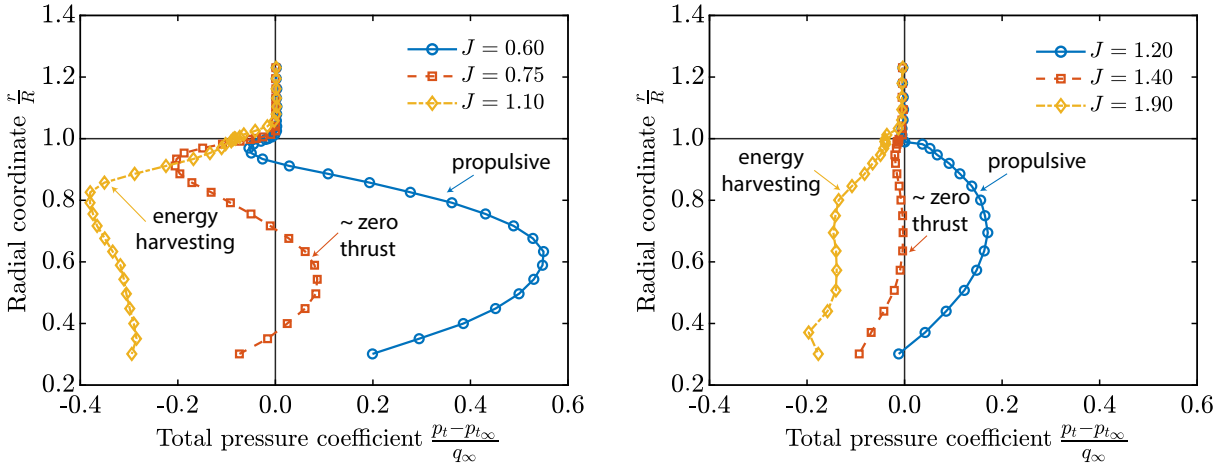

a) $\beta_{0.7R}$=15° b) $\beta_{0.7R}$=30°

Fig. 12 Total pressure coefficient distributions at $0.15R$ downstream of the propeller plane.

there is again a flat total pressure distribution, like for the lower pitch setting. The negative loading seems to increase slightly toward the root of the blades. Since the difference in output torque for the two pitch settings at the two mentioned energy-harvesting advance ratios was rather small (±20%) considering the large difference in total pressure values, and hence loading, it seems that, for $\beta_{0.7R} = 30°$, the propeller is more efficiently creating this negative torque, so with fewer losses in the form of negative thrust. This confirms the observed turbine efficiency, which is higher for $\beta_{0.7R} = 30°$ compared to $\beta_{0.7R} = 15°$, as was shown in Fig. 10a.

B. Blade-Sectional Flow Analysis

To better understand the observed blade loading in terms of the total pressure distribution behind the blades and to further investigate the flow phenomena around the blade sections that drive the propeller performance, the velocity fields around various blade sections are analyzed using the blade-sectional PIV data. Before the results are presented, it is relevant to discuss the observed flowfield in the obtained images, since the laser sheet was creating a lateral slice of the helicoidal vortex system in the slipstream. This means that the blade wake is passing this plane at different streamwise positions. The observed field of view is shown schematically in Fig. 13a, where also the approximate PIV camera positions are shown.

The wake of the blade section, at which the laser sheet is cutting, follows a helicoidal trajectory, meaning that it will move out of the image plane when traversing downstream. So when moving along the presumed propeller wake on the image plane (dashed black line), the wakes of blade sections that are above the cut radial position are passing through the measurement plane, indicated with the gray helicoidal lines. The wake filaments further downstream are shed earlier in time compared to the ones close to the blade section. Furthermore, these wakes are passing the measurement plane in an increasingly perpendicular manner (see Fig. 13b). As discussed in Sec. III, the laser sheet was not mirrored at the opposite side of the wind tunnel, and hence there is a shadow region in one of the camera's field of view due to the presence of the blade. Therefore, it was not possible to fully resolve the flowfield close to the blade sections.

When the phase-locked PIV data is analyzed, the stationary velocity field is derived. In the stationary frame, only the freestream velocity is present, which approaches the blade section from the front. However, to have a more logical flowfield around the blade sections, the rotational velocity is added to obtain the rotating reference frame [17,21]. Moving away from the blade in the y-direction leads to a larger blade radius. At the same time, when increasing the azimuthal angle, more of the local rotational velocity is oriented toward the vertical (out-of-plane) velocity component, leading to a constant rotational velocity that is added in the lateral direction in the measurement plane. The flowfields are shown for three radial sections that are equally spaced, namely sections 3, 6, and 8 as defined in Table 2, which are positioned at 90%, 69%, and 48% of the blade radius, respectively. The flowfields for these sections for $\beta_{0.7R} = 15°$ are shown in Fig. 14, while the flowfields for $\beta_{0.7R} = 30°$ are shown in Fig. 15, together with the local airfoil orientation at these specific radii. The total velocity flowfield in the rotating reference frame is presented, normalized with the local relative velocity ($V_{\text{rel}}^2 = V_\infty^2 + (\omega r)^2$). In the left top corner of each flowfield, the relative magnitude of the freestream and the rotational velocity are indicated. Note that a part of the flowfield is masked due to the presence of the blade and the laser shadow in the captured images.

1. $\beta_{0.7R} = 15°$

For section 3, which is located close to the tip ($r/R = 0.90$), the rotational velocity component is relatively large compared to the freestream velocity for both advance ratios. For the propulsive case (see Fig. 14a), this leads to a small negative angle of attack, but due to the camber of this blade section, there is still a larger acceleration of flow over the front side compared to the backside of the blade section, leading to positive lift and hence positive thrust, which corresponds to the small increase in total pressure at this radial location. On the backside of the blade, limited trailing edge separation is observed since a low-velocity region originates from the rear part of the blade section, merging with the boundary-layer flow from the front side. For the energy-harvesting case (see Fig. 14d), the reduction in the rotational velocity component makes the angle of attack more negative. The large acceleration of the flow after the leading edge, away from the surface indicates leading-edge separation, resulting in a small negative lift and hence negative thrust value. This illustrates the problem of operating the highly cambered and thin blade sections of the propeller in the energy-harvesting mode. The increase in drag associated with the separated flow could actually overcompensate the negative lift force in the torque direction, leading to a positive torque on the blade section. When the blade wake is observed, a wide region of decelerated flow is observed. The further decrease in velocity when traversing down the wake indicates that the blade sections above the analysis plane experience similar or worse flow conditions. The poor aerodynamic efficiency associated with the separated flow confirms the large total pressure loss observed in Fig. 12a close to the tip.

The flowfield around section 6 ($r/R = 0.69$), for the propulsive mode, can be seen in Fig. 14b. Here, the angle of attack is still negative, but less than for the previous blade section, leading to less acceleration of flow on the backside, increasing the positive thrust. Also, the trailing edge separation seems to be minimal on the backside, leading to a narrow and sharp blade wake. Since the local blade pitch is low, most of the lift is oriented in the thrust direction.

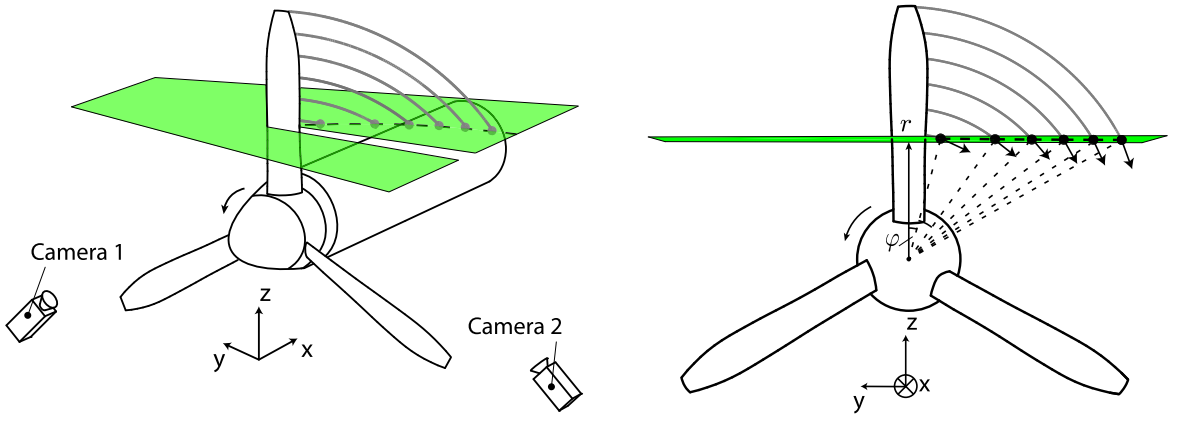

a) Isometric view including schematic helicoidal wake elements and approximate camera positions (not to scale)

b) Front view including relative radii and azimuthal angles of the different wake elements

Fig. 13 Schematic of the captured velocity field of the blade-sectional PIV analysis.

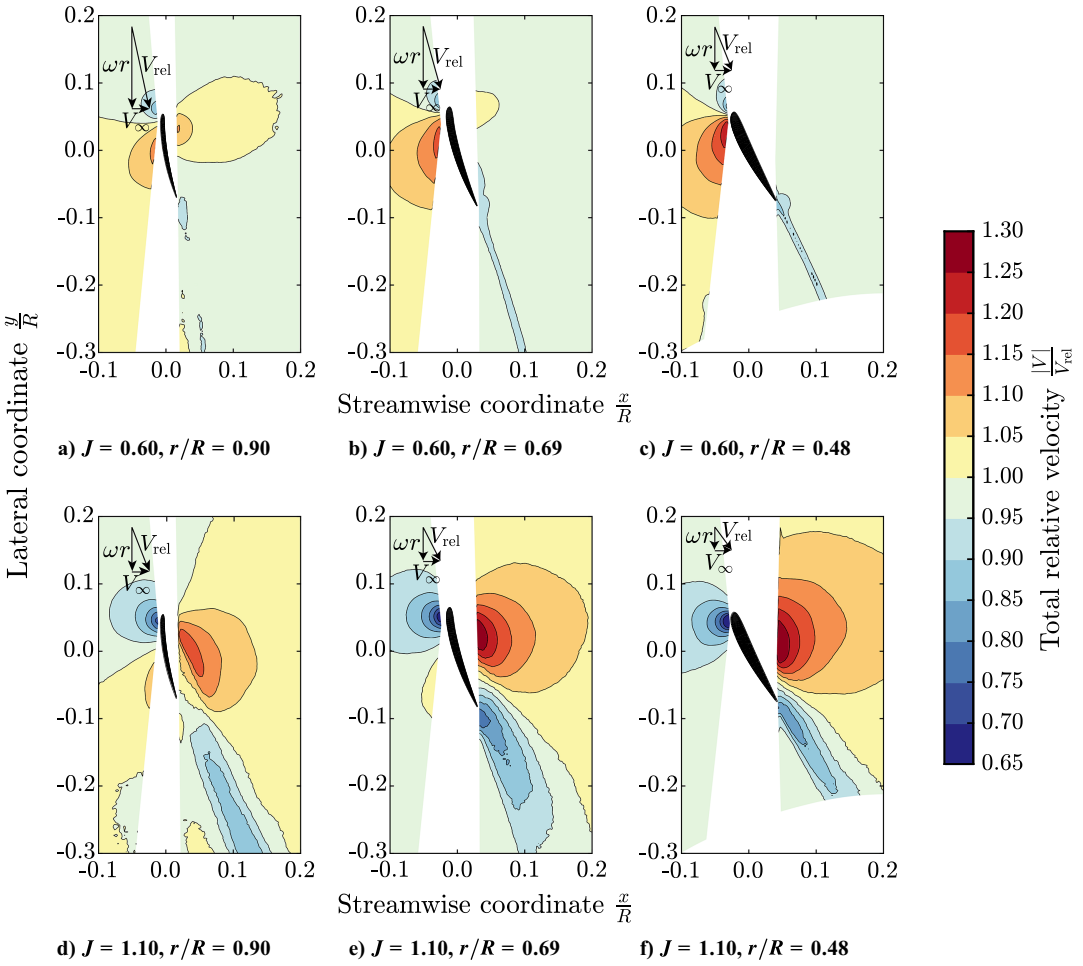

Fig. 14 Total relative velocity field around the blade sections for both propulsive ($J = 0.60$) and energy-harvesting ($J = 1.10$) conditions for $\beta_{0.7R} = 15°$.

This blade section is approximately at the point with the highest total pressure increase and the flow seems to be fully attached. For the energy-harvesting mode (see Fig. 14e), again separation is visible on the backside. However, the separation seems to be less intense than the previously discussed blade section and only occurs close to the trailing edge of the backside. The separated flow creates a wide region of decelerated flow. It is also possible that a laminar separation bubble is present [9,20], but since the flowfield very close to the blade surface could not be reconstructed, this cannot be confirmed. The region of decelerated flow on the front side and the acceleration over the backside result in negative lift, hence negative thrust and torque. Decreasing the camber would improve the energy-harvesting performance of this blade section; however, at the same time, it would decrease the performance in the propulsive mode.

Finally, the flowfield around blade section 8 ($r/R = 0.48$), for the propulsive mode, can be seen in Fig. 14c. Note that this velocity field was masked more, due to the obstruction of the nacelle. This blade section, closer to the blade root, is thicker and has less camber than the blade sections discussed before. The further reduction in the rotational velocity leads to a close to zero angle of attack. The flow seems to be fully attached, where a very narrow and sharp wake is present again. Due to the accelerated flow over the front side and limited acceleration over the backside, more positive lift is produced than before. However, this force is also oriented more into the torque direction than for section 6. For the energy-harvesting case (see Fig. 14f), the flowfield is comparable to that of section 6. The trailing edge separation seems to be reduced further on the backside compared to the previous blade section and the wake is less wide. Therefore, the region of accelerated flow is increased, increasing the negative lift. As for the propulsive case, this lift vector is more oriented in the torque direction, which is now beneficial for the energy-harvesting operation, since more power can be extracted.

2. $\beta_{0.7R} = 30°$

The higher pitch setting of $\beta_{0.7R} = 30°$ is closer to the design pitch setting of this propeller, leading to angles of attack on the blade sections that are close to zero. The three considered blade sections show positive loading in the propulsive regime ($J = 1.20$), as can be seen in Figs. 15a–15c. Note that due to the higher pitch setting, the shadow region of the blade increased in the measurement plane, and therefore more area had to be masked. For this pitch setting, the relative incoming velocity is better aligned with the local blade pitch than for $\beta_{0.7R} = 15°$ and therefore no negative loading is observed anywhere along the blade, confirming the observed total pressure distribution. Due to the proper alignment of the incoming flow, it seems that there is no trailing edge separation at any of the analyzed radial sections, leading again to a thin and sharply defined blade wake. The velocity fields around the three sections are rather similar, especially those for section 6 ($r/R = 0.69$) and section 8 ($r/R = 0.48$). However, due to the local inflow angle, the loading is oriented more into the direction of the thrust for sections closer to the tip, and combined with the higher effective velocity, section 6 generates more thrust than section 8, resulting in a higher total pressure increase for the former, as was shown in Fig. 12b.

For the energy-harvesting condition ($J = 1.90$), the flowfields can be seen in Figs. 15d–15f for section 3 ($r/R = 0.90$), section 6 ($r/R = 0.69$), and section 8 ($r/R = 0.48$), respectively. For all analyzed sections, the large acceleration over the backside, combined with the deceleration over the front part of the blade, means that the blade sections do create negative lift and hence negative

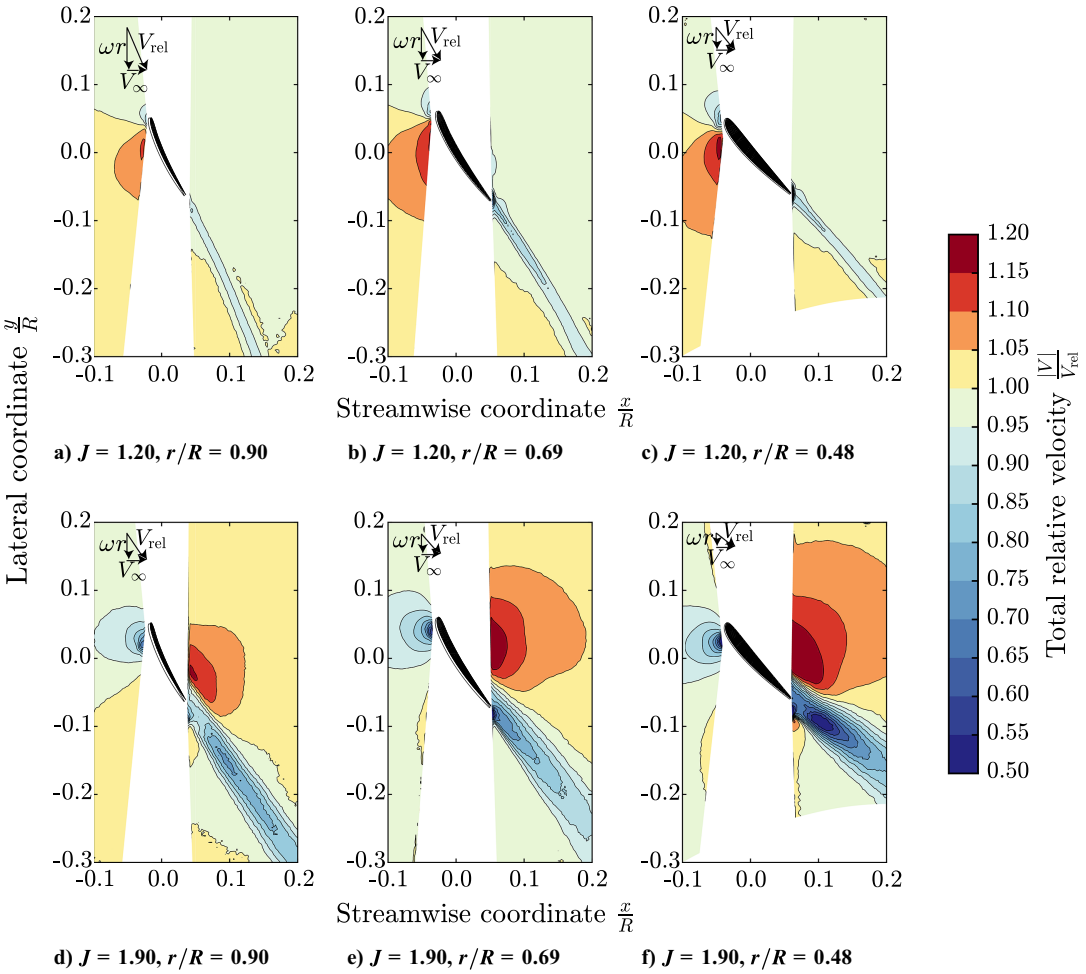

Fig. 15 Total relative velocity field around the blade sections for both propulsive ($J = 1.20$) and energy-harvesting ($J = 1.90$) conditions for $\beta_{0.7R} = 30°$.

thrust and torque. Furthermore, there seems to be trailing edge separation, indicated by the wide blade wake, where a large deceleration of the flow is present. As discussed in Sec. V.A, for $\beta_{0.7R} = 30°$, the tip region experiences smaller (negative) angles of attack, while the root sections experience more negative angles of attack than for $\beta_{0.7R} = 15°$. From the observed flowfields, leading-edge separation does not seem to occur for the tip region (Fig. 15d), as was the case for the lower pitch setting, due to the improved flow alignment with the local blade sections. For the case of $\beta_{0.7R} = 15°$, the trailing edge separation seems to have reduced when moving toward the root. However, for the higher pitch setting, it seemed to have increased toward the root. Figure 15f shows a very large declaration in the separated region compared to the other sections. This explains the increase in total pressure loss when moving inboard, as shown in Fig. 12b. For the sections located more inboard, the larger inflow angle does result in a negative lift vector, which is more oriented in the negative torque direction. Therefore, the higher pitch setting can convert the negative loading more efficiently into negative torque, increasing the turbine efficiency compared to the lower pitch setting.

To conclude, due to the highly cambered, thin airfoils at the tip region of the blade, the flow separates from the leading edge of the blade sections for the case of $\beta_{0.7R} = 15°$. For the higher pitch setting ($\beta_{0.7R} = 30°$), the flow is better aligned with the blade sections at the tip, reducing the leading-edge stall. However, trailing edge separation still is present over the whole blade, reducing the aerodynamic performance of the blade sections at negative angles of attack, limiting both the negative thrust and torque for the energy-harvesting mode. This ultimately also limits the total power that is extracted from the flow, contributing to the low energy-harvesting efficiency observed before. For $\beta_{0.7R} = 15°$, the blade sections located toward the root show more attached flow, meaning that they operate more efficiently as a wind turbine blade section. However, due to the local inflow angle, most of the negative lift generated at the blade section is oriented in the thrust direction, not adding to the torque. For $\beta_{0.7R} = 30°$, the negative loading is better aligned with the torque direction than for the lower pitch setting, causing an increase in turbine efficiency, as observed in Fig. 10a. However, the trailing edge separation increases toward the root, reducing the aerodynamic performance of the blade section. Due to the higher advance ratio and hence lower effective velocity at the energy-harvesting condition, compared to the low pitch setting, the output power is lower than for $\beta_{0.7R} = 15°$.

A possible redesign of the conventional propellers could be performed to improve the energy-harvesting operation. By reducing the camber of the propeller blade sections, less flow separation will occur at negative angles of attack, potentially increasing the energy-harvesting output. When symmetric airfoil sections are used, similar propeller and turbine efficiencies can be obtained [4]. However, decreasing the camber of a propeller blade, which is optimized for propulsive conditions, will lead to a decrease in propeller efficiency. This means that the flight phases where the propeller is used in propulsive mode consume more energy. Since the direction of the camber needed for a propeller and wind turbine blade are opposite, there is always a compromise between the two modes. Furthermore, as shown in Figs. 9 and 10, there is a difference between operating the propeller at a high turbine efficiency or a high energy-harvesting efficiency. The design for a high turbine efficiency might not lead to maximum energy-harvesting output. Depending on the mission profile and length of the separate mission segments, the propeller should be designed accordingly, such that the overall energy consumption can be minimized.

VI. Slipstream-Induced Velocities

Now the integrated performance and blade sectional characteristics are discussed, it is important to relate the change in propeller operation to the observed flowfield behind the propeller since this will greatly affect the interaction with downstream lifting surfaces. Therefore, the velocity components in the propeller slipstream were analyzed for both propulsive and energy-harvesting conditions. In this way, the local axial and tangential induction can be related to the forces on the blade sections. To analyze the velocity distributions in the slipstream, both phase-averaged and phase-locked PIV were performed. For the discussion of the PIV results, the propulsive and the energy-harvesting modes were considered. The zero-thrust case was left out of the discussion since the induced velocities will be small for this condition. In Sec. VI.A the phase-averaged results are discussed, and in Sec. VI.B, the phase-locked results are presented. Upstream and downstream of the blades, the flowfield was masked over $0.05R$ since no accurate correlations could be found here due to the presence of the blades and reflections off their surface. Furthermore, part of the velocity field close to the nacelle was removed, due to laser reflections off the surface, meaning that velocity data is only present from $r/R = 0.36$ onward.

A. Phase-Averaged Velocity Field

The slipstream flowfields obtained by the phase-averaged PIV results give insight into the correlation between the blade loading and the trailing propeller flowfield. Furthermore, the velocity components inside the slipstream are relevant for a downstream element positioned inside the slipstream, such as a wing.

1. $\beta_{0.7R} = 15°$

The data for $\beta_{0.7R} = 15°$ are presented in Fig. 16. The propulsive mode shows an increase in axial velocity in the slipstream compared to the freestream (see Fig. 16a). Behind the tip, there is a small region of decelerated flow associated with the outboard negative loading, which agrees with the negative loading observed with the five-hole probe (Fig. 12a). The inner part of the slipstream reflects the positively loaded part of the blade and shows a contracting slipstream behind it. This contraction leads to a further acceleration of the axial velocity in the streamwise direction. The radial distribution of axial velocity is presented for four different streamwise locations in Fig. 16e, where $x/R = 0.25, 0.50, 0.75,$ and 1.00. Here, the acceleration of the positively loaded blade region is confirmed. However, the tip region, which shows a negative induction, does not present a further deceleration in the streamwise direction. There seems to be a mixing of higher momentum flow from the surrounding regions and this lower momentum region due to the propeller tip vortex.

In Fig. 16b, the axial velocity field of the propeller is shown for $J = 1.10$. There is a reduction in axial velocity compared to the freestream, which would yield a reduction in lift of any lifting surface submerged into the slipstream. The largest reduction in axial velocity is found at the location where the highest total pressure loss was observed in the pressure measurements (see Fig. 12a). This peak is at 85% of the blade radius, at which the minimum axial velocity is around 0.83 times the freestream velocity. As shown in Fig. 14d, the blade sections close to the blade tip feature large separated flow regions, which cause this large reduction of the axial velocity observed in the slipstream. When moving more inboard, less separation was observed around the blade sections, which means that the reduction in axial velocity is smaller compared to the peak values. When the axial velocity is examined along radial lines at different streamwise positions (see Fig. 16e), the shape is again similar to the observed total pressure distributions. For the energy-harvesting mode, the slipstream is only expanding marginally, where the further deceleration of the axial velocity downstream of the blades is limited. This is also visible in the radial distributions, where the four curves cross the y-axis at the same place. This is different from the propulsive case, where the additional increase in axial velocity was more clear. This is a further indication that most outboard blade sections feature separated flow, which limits the amount of expansion.

Next to the axial velocity component, which is coupled to the generated thrust, the tangential velocity or swirl component was analyzed, which relates to the torque on the blades. During the experiment, the propeller was rotating into the plane, meaning that the swirl component in the propulsive mode is negative in the used reference system, which corresponds to a positive torque. The change in swirl direction when switching from propulsive to the energy-harvesting mode will also invert the swirl effects on a lifting surface behind the propeller. This can be disadvantageous for wing-mounted propellers, where the swirl recovery may become less beneficial. The tangential velocity field for the propulsive condition ($J = 0.60$) can be seen in Fig. 16c. The highest swirl velocities are measured at the root section of the blade. When the slipstream contraction or expansion is limited, the swirl velocities marginally change when traversing downstream. The radial distributions of swirl velocity along the four analysis lines are shown in Fig. 16f. The swirl distribution for the propulsive case shows that much less torque is located toward the tip, whereas normally the torque distribution is rather flat over a large part of the blade [10]. The negative angles of attack and the associated reduction in positive lift lead to a reduction in torque, together with the fact that the lift is pointing more in the direction of thrust.

For the energy-harvesting case ($J = 1.10$), the negative torque on the blade sections results in a negative induction and hence a swirl velocity with the opposite sign compared to the propulsive case. The tangential velocity field for the energy-harvesting case can be seen in Fig. 16d. The tangential velocity is largest near the root and becomes smaller toward the tip. For the attached flow, the negative lift force on the blade sections is the main component that determines the negative torque. Furthermore, for the blade sections located close to the root, the negative lift is directed more toward the torque component compared to the section closer to the tip. From 85% of the radius onward, there is a sharp drop in the swirl velocity, and at the tip, the swirl velocity actually is negative, meaning that the drag force of the blade sections, which contribute positively to torque, starts to outweigh the negative lift in the opposite direction (see Fig. 1). This is an indication of blade sections that are completely stalled due to the large negative angles of attack on the thin, cambered airfoils, which was confirmed in Fig. 14d. The radial distributions of swirl velocity, as shown in Fig. 16f, show that this velocity component actually keeps on increasing toward the blade root. Together with the axial velocity distribution, it can be confirmed that the root sections operate aerodynamically more efficiently, with flow still attached, compared to the outboard blade sections, which was also observed in Figs. 14e and 14f. The increase in negative tangential induction results from the negative lift force that is pointing increasingly more in the direction of the negative torque. So the peak of the negative lift force will be close to the root of the blade.

2. $\beta_{0.7R} = 30°$

In Fig. 17, the same data are shown for the case of $\beta_{0.7R} = 30°$. Since the loading in the blades is much lower for this pitch setting, due to the higher advance ratios, the maximum and minimum values of the axial induction are lower; see Figs. 17a and 17b for the propulsive ($J = 1.20$) and energy-harvesting mode ($J = 1.90$), respectively. The axial velocity field for the propulsive case is similar to the lower pitch setting. When examining the radial velocity distributions (see Fig. 17e), a similar shape is observed as for $\beta_{0.7R} = 15°$, but the peak of the axial induction is moved slightly upward, to about 70% of the blade radius. For this pitch setting, which is closer to the design pitch setting, the tip region is positively loaded, since the local velocity vector is better aligned with the local blade pitch. This was also shown in the total pressure distribution behind the blades and in the flowfield around the blade section at $r/R = 90$ (Fig. 15a). The fact that the whole blade is producing positive thrust, combined with the lower induction losses, increases the propeller efficiency compared to $\beta_{0.7R} = 15°$, as was observed in Fig. 9a.

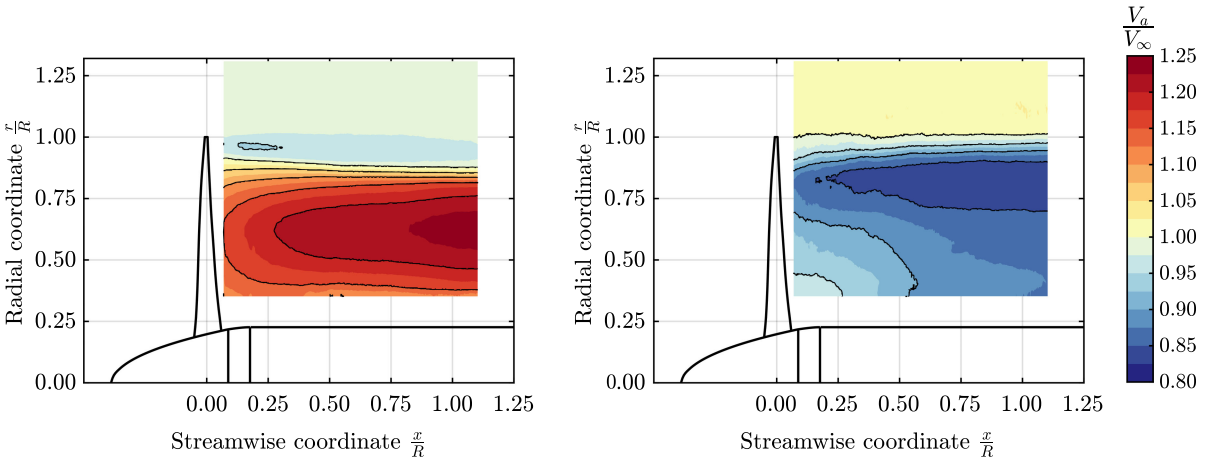

a) Axial velocity field for $J = 0.60$ (propulsive)

b) Axial velocity field for $J = 1.10$ (energy harvesting)

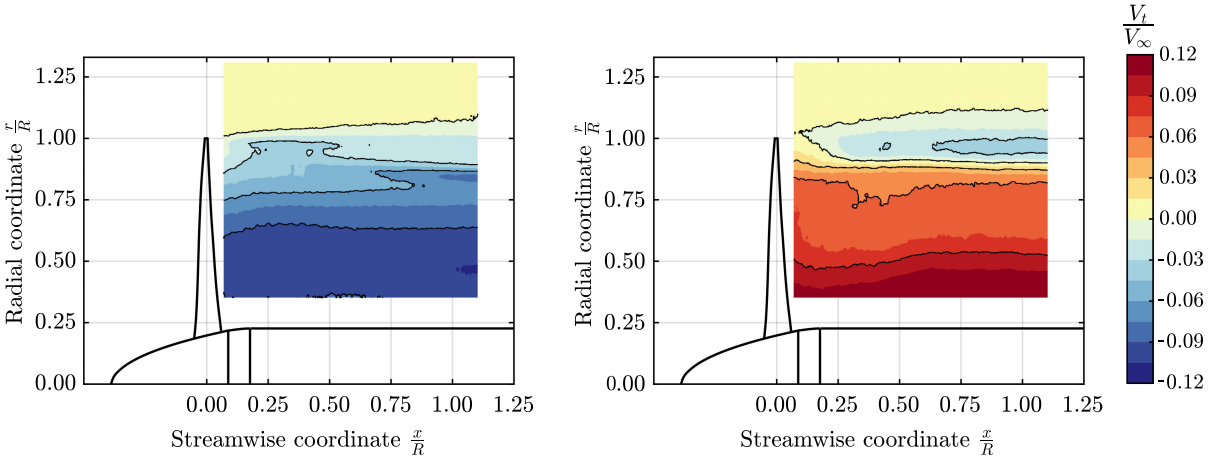

c) Tangential velocity field for $J = 0.60$ (propulsive)

d) Tangential velocity field for $J = 1.10$ (energy harvesting)

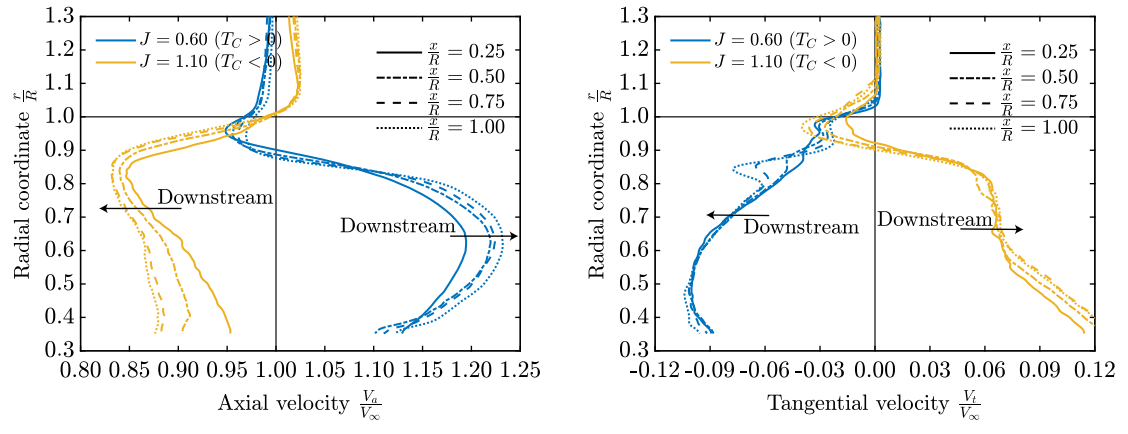

e) Axial velocity distribution along radial lines

f) Tangential velocity distribution along radial lines

Fig. 16 Phase-averaged velocity fields in the propeller slipstream for $\beta_{0.7R} = 15°$.

For the energy-harvesting mode ($J = 1.90$), the flowfield of the axial velocity shows more irregularities. When looking at the axial velocity distributions (Fig. 17e), the value of the axial induction shoots up close to the root, surpassing the local maximum value at around 80% of the blade radius for the three most downstream analysis lines. This indicates an increase in loading compared to the blade sections around 50% of the blade radius, which was also observed by the kink in the total pressure distribution at around 40% blade radius. For the blade section at $r/R = 0.48$ (Fig. 15f), it was shown that there was an increased trailing edge separation compared to the blade section at $r/R = 0.69$. This increase in trailing edge separation leads to a reduction in negative lift, explaining the observed reduction in negative axial induction when moving more inboard. Therefore, the sudden increase in negative axial induction for the blade sections located closer to the root, compared to that at $r/R = 0.48$, means that there is again an increase in negative lift, increasing the negative thrust. This might be caused by the reduction in trailing edge separation for these blade sections compared to the section above. Another possibility is the existence of a laminar separation bubble on the blade sections around 50% of the blade [9,20], which would not be present at the blade sections closest to the root, increasing their performance at negative angles of attack.

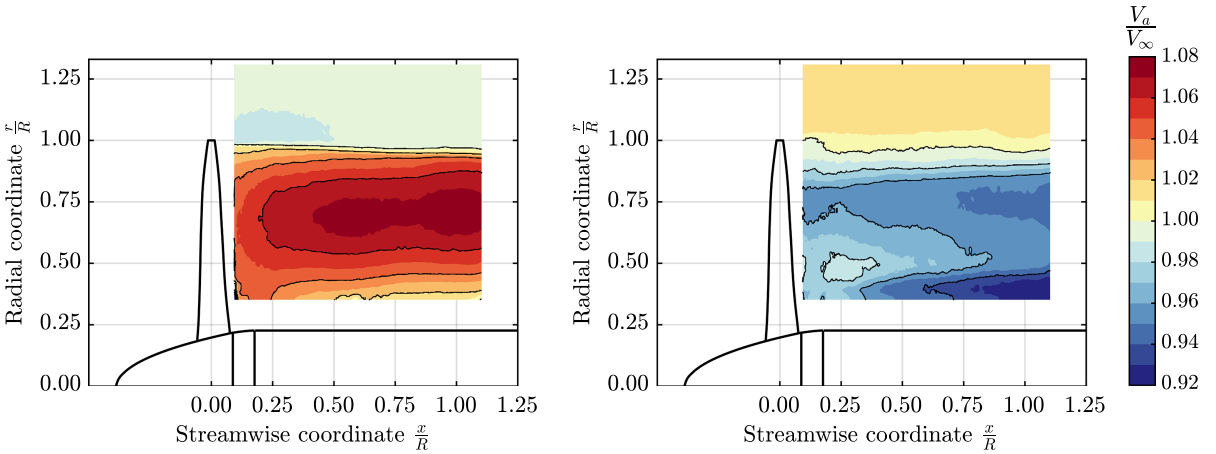

a) Axial velocity field for $J = 1.20$ (propulsive)

b) Axial velocity field for $J = 1.90$ (energy harvesting)

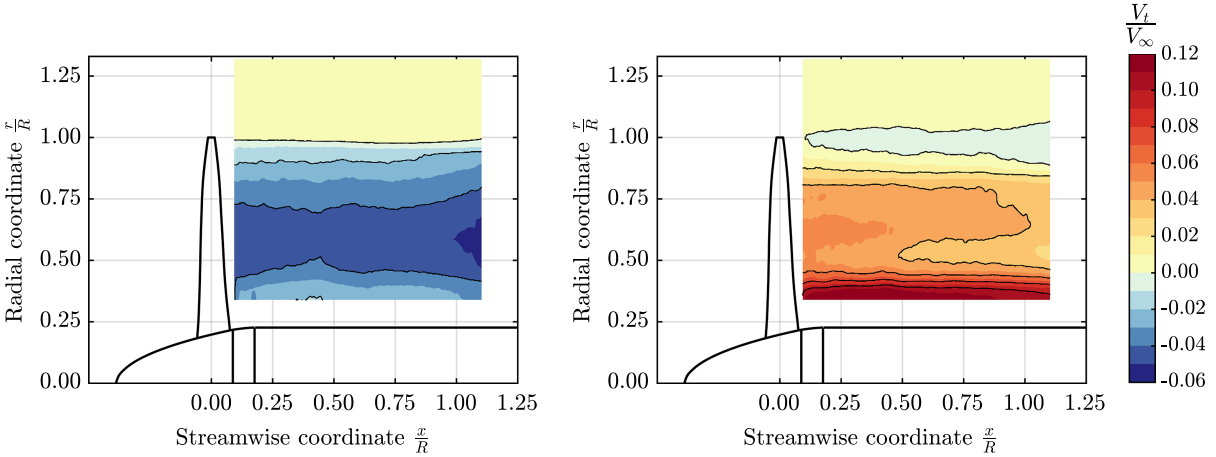

c) Tangential velocity field for $J = 1.20$ (propulsive)

d) Tangential velocity field for $J = 1.90$ (energy harvesting)

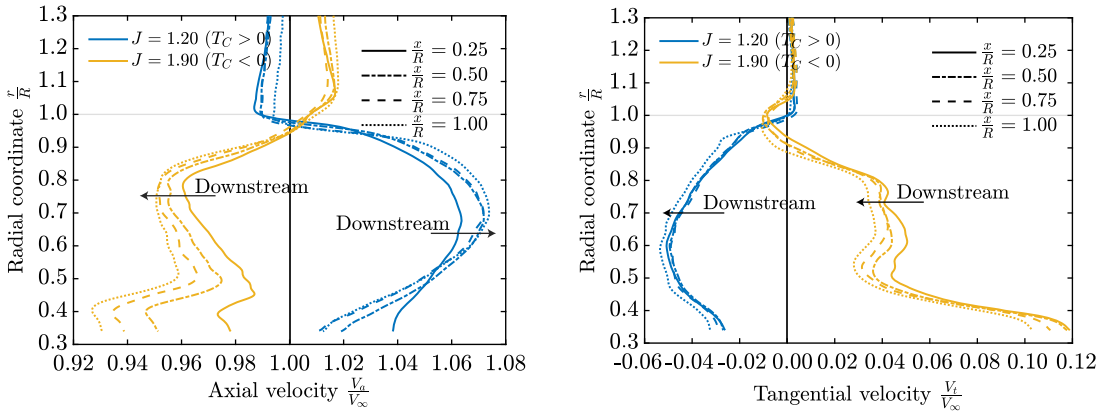

e) Axial velocity distribution along radial lines

f) Tangential velocity distribution along radial lines

Fig. 17 Phase-averaged velocity fields in the propeller slipstream for $\beta_{0.7R} = 30°$.

The swirl velocity field is shown in Figs. 17c and 17d for the propulsive ($J = 1.20$) and energy-harvesting mode ($J = 1.90$), respectively. Again, for the propulsive case, there is not much difference in the observed flowfield compared to the lower pitch setting. The swirl velocity peaks on the inboard side and remains more flat than for $\beta_{0.7R} = 15°$, showing a more conventional torque distribution (see Fig. 17f). This is also because, for a higher pitch setting, the lift force is more directed into the torque direction compared to the lower pitch setting. Due to the limited contraction or expansion, there is hardly any change in the swirl velocity when traversing downstream. As mentioned before, the tip region is not negatively loaded as was the case for $J = 0.60$, and hence only positive torque is observed, leading to negative swirl velocities in the used reference frame. The swirl velocity field of $J = 1.90$ shows negative values at the tip, similar to $\beta_{0.7R} = 15°$, indicating that positive torque is required, while these blade sections create negative thrust. The large gradient near the root of the blade corresponds to the sudden increase in negative lift, concluding the aerodynamic performance of these blade sections is improved, as was discussed before. The values of the tangential induction are similar to that of $\beta_{0.7R} = 15°$ at $J = 1.10$ (see Fig. 16f). So the amount of torque that is generated on these root sections is similar between the different pitch settings, despite the

much lower dynamic pressure for $\beta_{0.7R} = 30°$, which means that the conditions here are more optimal for energy harvesting. The associated negative induction and hence negative thrust are much smaller, which results in the higher turbine efficiency for the high pitch setting. However, due to the lower rotational speed, the output power is lower than for $\beta_{0.7R} = 15°$.

B. Phase-Locked Velocity Field

To complete the link between the observed integrated performance and the flow phenomena around the propeller blades, the phase-locked PIV data are discussed. The unsteady phase-dependent flowfields might be relevant when studying the unsteady interaction phenomena for the propeller-installed configuration. To relate to expected phenomena in terms of periodic unsteady loads on a downstream surface, it was chosen to show the normalized z-vorticity value ($\omega_z D/V_\infty$) in the slipstream to highlight the blade wake and blade vortices. The phase-locked analysis is presented for $\beta_{0.7R} = 15°$, where the data for $\beta_{0.7R} = 30°$ did not show a relevant phase-locked flowfield for all the tested advance ratios. This was due to the relatively low rotational speed at the higher advance ratios for the higher blade pitch. Therefore, the wake of the blade turned out to be outside the field of view at the used phase-locked blade azimuthal angle. The data for $\beta_{0.7R} = 15°$ are presented in Figs. 18a and 18b for the propulsive ($J = 0.60$) and the energy-harvesting mode ($J = 1.10$), respectively. Since the advance ratio is higher for the energy-harvesting condition, the pitch angle of the helicoidal wake is higher than for the propulsive case. This means that, for $J = 1.10$, the wake is convected more downstream during a single rotation of the propeller than for $J = 0.60$. Therefore, for the propulsive mode, two blade wakes were present in the analyzed field of view, while for the energy-harvesting mode, only one blade wake was present.

For the propulsive mode, the blade wakes show a similar shape as the axial velocity profiles observed behind the blade (Fig. 16e). The contraction of the slipstream is visible since the blade wake becomes more curved and moves inboard while traversing downstream. At around 60% of the blade radius, where the largest axial induction was observed, the most deformation of the blade wake occurs. The blade wake is relatively small and has distinctive boundaries, which means that the lifting surface submerged in the slipstream will experience a steady periodic fluctuation of the loads. The negative tip loading observed in the total pressure data is also recognized in the velocity fields, indicated by the negative vorticity. For a regular propulsive operating condition, the loading would be positive over the entire blade span, and hence a single tip vortex would be positioned at the edge of the slipstream. However, due to the negative loading at the tip, this "tip" vortex is located more inboard. Furthermore, the circulation gradients are reduced due to the low loading, reducing the strength of the vortices that are being shed here.

For the energy-harvesting mode, the wake of the blades is much less clearly defined than for the propulsive case, which is due to the lower loading gradients on the blade. Especially on the inboard side of the propeller, the loading gradients are small, and therefore the velocity gradients in the slipstream are also much smaller compared to the propulsive mode. As was observed in the total pressure distribution behind the blades (Fig. 12a), only the tip region contained large loading gradients, resulting in a clearly defined top vortex. For a lifting surface submerged in the slipstream, the periodic fluctuations are much less intense, combined with the fact that the frequency of the blade wake is lower, due to the change in advance ratio, compared to the propulsive mode. This could be beneficial for the unsteadiness in the loading of these lifting surfaces. However, these vorticity fields by PIV are averaged over time, which means that broadband fluctuations are not visible in the flowfield. It could be that the blade wake of the propeller at energy-harvesting conditions contains more unsteady fluctuations, resulting in more unpredictable load variations compared to the propulsive conditions.

VII. Conclusions

The purpose of this paper was to quantify the aerodynamic performance of a three-bladed propeller that was operated at both positive and negative thrust and power conditions. Furthermore, the dominant flow phenomena that drive the off-design performance while the propeller operates in the energy-harvesting mode were to be understood and quantified using blade loading distributions in terms of total pressure and flowfields obtained using PIV. Based on the results, the following conclusions were drawn:

1) In the energy-harvesting regime, the negative thrust and power peak at a specific advance ratio, after which they do not decrease further with increasing advance ratio due to the increasingly more negative angles of attack on the blade sections. Since the propeller was designed for propulsive operations and hence not for energy-harvesting operations, the camber is in the opposite direction when considering energy-harvesting operations. The highly cambered blade sections are prone to separation in the energy-harvesting mode, limiting the performance.

2) Due to the negative angles of attack on the highly cambered blade sections and associated flow separation, the maximum energy-harvesting efficiency was limited to around 11% for $\beta_{0.7R} = 15°$, which is rather low compared to equivalent wind turbines. Increasing the blade pitch setting reduces this energy-harvesting efficiency even further, where $\beta_{0.7R} = 30°$ only showed a 6% maximum efficiency in the energy-harvesting mode. Even though the output torque of the high pitch setting was only around 20% less than that of the low pitch setting, the point of maximum energy harvesting for the high pitch setting is achieved at a higher

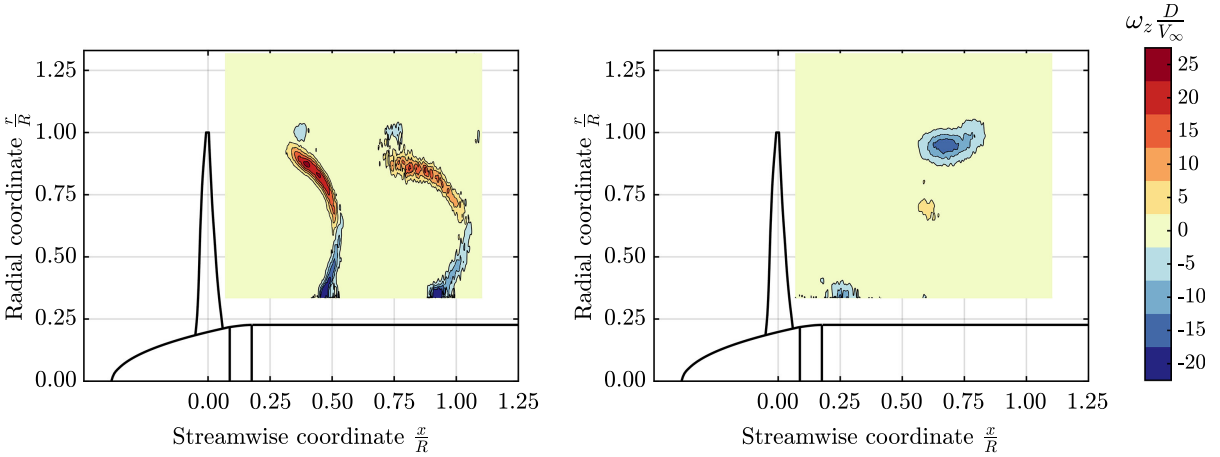

a) $J = 0.60$ (propulsive) **b) $J = 1.10$ (energy harvesting)**

Fig. 18 Phase-locked vorticity fields in the propeller slipstream for $\beta_{0.7R} = 15°$ for the propulsive and energy-harvesting conditions.

advance ratio than the low pitch setting, leading to the large difference in output power.

3) The energy-harvesting efficiency at low pitch settings comes at a cost of high negative thrust. The turbine efficiency, which is a measure of the propeller's ability to convert negative loading into output power, is lower at this low pitch setting than for the high pitch setting. Increasing the pitch setting leads to an increase in turbine efficiency, although this means lowering the maximum energy-harvesting power output. For low values of allowable negative thrust, the most power can actually be harvested by using a high pitch setting.

4) If the propeller angle of attack is not zero (straight inflow), the integrated performance is changed. At both propeller pitch settings, at the analyzed advance ratios, the propeller thrust becomes more positive when increasing the angle of attack for the propulsive mode. At the same time, the thrust becomes less negative when increasing the angle of attack for the energy-harvesting mode at both pitch settings. The same happens for the power of the propeller, which becomes more positive and less negative when increasing the angle of attack, for the propulsive and energy-harvesting mode, respectively. This means that, for the energy-harvesting mode, the energy-harvesting efficiency is reduced even further. For the propulsive mode, the increase in thrust is more dominant than the increase in power, leading to an improved propeller efficiency. However, for the energy-harvesting mode, the reduction in output power is larger than the reduction in negative thrust, decreasing the turbine efficiency.

5) For $\beta_{0.7R} = 15°$, the flowfield around the highly cambered blade sections at the tip showed large separated flow regions, which is caused by the high negative angle of attack in the energy-harvesting mode. The blade sections located more toward the root are thicker and less cambered, reducing the separated flow and hence improving the energy-harvesting capabilities. For $\beta_{0.7R} = 30°$, the radial distribution of the angle of attack on the blade sections is changed at the energy-harvesting mode, compared to the low pitch setting. For the blade sections at the tip, there are less negative angles of attack, reducing the flow separation.

6) The axial and tangential velocity fields also show stalled blade sections at the tip region for both pitch settings in energy-harvesting conditions. Most of the negative torque and hence power are generated close to the root, which means that the thicker root sections operate better with the negative angles of attack compared to the thinner midspan and tip sections. Furthermore, the higher local flow angles at the root increase the negative lift contribution in the direction of the torque, increasing the local tangential induction.

7) The phase-locked PIV showed a distinctive blade wake and tip vortex for the propulsive mode. However, due to the lower loading gradients, the velocity gradients in the slipstream for the energy-harvesting mode are lower, and the blade wake is, therefore, less apparent. This results in more spread-out, unsteady velocity fluctuations in the slipstream.

The results obtained in this paper increase the knowledge of the operation of propellers at energy-harvesting conditions. In this paper, the focus was put on the energy-harvesting performance, but operating a propeller in energy-harvesting conditions can also be done to improve control and stability, or the propeller could be used as an alternative airbrake. This more flexible operation of propellers may help to unlock performance enhancements of future electric aircraft.

Acknowledgments

The research leading to these results is part of the FUTPRINT50 project. This project has received funding from the European Union's Horizon 2020 Research and Innovation program under Grant Agreement No. 875551.

References

[1] Hepperle, M., "Electric Flight—Potential and Limitations," *Energy Efficient Technologies and Concepts of Operation Workshop*, STO-MP-AVT 209, 2012, https://elib.dlr.de/78726/1/MP-AVT-209-09.pdf.

[2] Moore, M. D., and Fredericks, B., "Misconceptions of Electric Propulsion Aircraft and their Emergent Aviation Markets," *52nd Aerospace Sciences Meeting*, AIAA Paper 2014-0535, 2014. https://doi.org/10.2514/6.2014-0535

[3] Barnes, J. P., "Flight Without Fuel—Regenerative Soaring Feasibility Study," *General Aviation Technology Conference & Exhibition*, SAE Paper 2006-01-2422, 2006. https://doi.org/10.4271/2006-01-2422

[4] Barnes, J. P., "Regenerative Electric Flight: Synergy and Integration of Dual-Role Machines," *53rd AIAA Aerospace Sciences Meeting*, AIAA Paper 2015-1302, 2015. https://doi.org/10.2514/6.2015-1302

[5] Eržen, D., Andrejašič, M., Lapuh, R., Tomažič, J., Gorup, Č., and Kosel, T., "An Optimal Propeller Design for In-Flight Power Recuperation on an Electric Aircraft," *Aviation Technology, Integration, and Operations Conference*, AIAA Paper 2018-3206, 2018. https://doi.org/10.2514/6.2018-3206

[6] Cherubini, A., Papini, A., Vertechy, R., and Fontana, M., "Airborne Wind Energy Systems: A Review of the Technologies," *Renewable and Sustainable Energy Reviews*, Vol. 51, Nov. 2015, pp. 1461–1476. https://doi.org/10.1016/j.rser.2015.07.053

[7] Echeverri, P., Fricke, T., Homsy, G., and Tucker, N., The Energy Kite: Selected Results From the Design, Development and Testing of Makani's Airborne Wind Turbines. Part II, Technical Artifacts," Makani Technologies LLC TR, 2020, https://storage.googleapis.com/x-prod.appspot.com/files/Makani_TheEnergyKiteReport_Part2.pdf.

[8] Alvarez, E. J., Mehr, J., and Ning, A., "FLOWUnsteady: An Interactional Aerodynamics Solver for Multirotor Aircraft and Wind Energy," *AIAA AVIATION Forum*, AIAA Paper 2022-3218, 2022. https://doi.org/10.2514/6.2022-3218

[9] Goyal, J., Sinnige, T., Avallone, F., and Ferreira, C., "Benchmarking of Aerodynamic Models for Isolated Propellers Operating at Positive and Negative Thrust," *AIAA Journal*, Vol. 62, No. 10, 2024, pp. 3,758–3,775. https://doi.org/10.2514/1.J064093

[10] Sinnige, T., Stokkermans, T. C. A., van Arnhem, N., and Veldhuis, L. L. M., "Aerodynamic Performance of a Wingtip-Mounted Tractor Propeller Configuration in Windmilling and Energy-Harvesting Conditions," *AIAA Aviation Forum*, AIAA Paper 2019-3033, 2019. https://doi.org/10.2514/6.2019-3033

[11] Mayntz, J., Keimer, J., Tegtmeyer, P., Dahmann, P., Hille, S., Stumpf, E., Fisher, A., and Dorrington, G., "Aerodynamic Investigation on Efficient Inflight Transition of a Propeller from Propulsion to Regeneration Mode," *AIAA SCITECH Forum*, AIAA Paper 2022-0546, 2022. https://doi.org/10.2514/6.2022-0546

[12] Dobbinga, E., and van Ghesel Grothe, J. A., "De Lage-Snehlheids Windtunnel Van De Sub-Afd. Vliegtuigbouwkunde Der Technische Hogeschool," Delft Univ. of Technology TR VTH-77, 1955, https://repository.tudelft.nl/record/uuid:dbf0b1e4-f765-439f-9acd-309de527d2c7.

[13] Li, Q., Öztürk, K., Sinnige, T., Ragni, D., Wang, Y., Eitelberg, G., and Veldhuis, L. L. M., "Design and Experimental Validation of Swirl Recovery Vanes for Propeller Propulsion Systems," *AIAA Journal*, Vol. 56, No. 12, 2018, pp. 4719–4729. https://doi.org/10.2514/1.J057113

[14] Nederlof, R., Ragni, D., and Sinnige, T., "TUD-XPROP-3 Propeller Geometry," *Zenodo*, 2024. https://doi.org/10.5281/zenodo.13645390

[15] Stokkermans, T. C. A., Usai, D., Sinnige, T., and Veldhuis, L. L. M., "Aerodynamic Interaction Effects Between Propellers in Typical eVTOL Vehicle Configurations," *Journal of Aircraft*, Vol. 58, No. 4, 2021, pp. 815–833. https://doi.org/10.2514/1.C035814

[16] Veldhuis, L. L. M., "Propeller Wing Aerodynamic Interference," Ph.D. Thesis, Faculty of Aerospace Engineering, Delft Univ. of Technology, Delft, The Netherlands, 2005, https://repository.tudelft.nl/islandora/object/uuid%3A8ffbde9c-b483-40de-90e0-97095202fbe3.

[17] Ragni, D., and van Oudheusden, B. W., "Non-Intrusive Aerodynamic Loads Analysis of an Aircraft Propeller Blade," *Experiments in Fluids*, Vol. 51, No. 2, 2011, pp. 361–371. https://doi.org/10.1007/s00348-011-1057-7

[18] Goyal, J., Sinnige, T., Avallone, F., and Ferreira, C., "Aerodynamic and Aeroacoustic Characteristics of an Isolated Propeller at Positive and Negative Thrust," *AIAA AVIATION Forum*, AIAA Paper 2021-2187, 2021. https://doi.org/10.2514/6.2021-2187

[19] Sinnige, T., van Arnhem, N., Stokkermans, T. C. A., Eitelberg, G., and Veldhuis, L. L. M., "Wingtip-Mounted Propellers: Aerodynamic

Analysis of Interaction Effects and Comparison with Conventional Layout," *Journal of Aircraft*, Vol. 56, No. 1, 2019, pp. 295–312. https://doi.org/10.2514/1.C034978

[20] Goyal, J., Avallone, F., and Sinnige, T., "Isolated Propeller Aeroacoustics at Positive and Negative Thrust," *Aerospace Science and Technology*, Vol. 147, April 2024, Paper 109021. https://doi.org/10.1016/j.ast.2024.109021

[21] del Campo, V., Ragni, D., Micallef, D., Akay, B., Diez, F. J., and Ferreira, C. Simão, "3D Load Estimation on a Horizontal Axis Wind Turbine Using SPIV," *Wind Energy*, Vol. 17, No. 11, 2014, pp. 1645–1657. https://doi.org/10.1002/we.1658

A. Gopalarathnam
Associate Editor